Micromechanical Behaviour in Shearing of Reproduced Flat LBS Grains with Strong and Weak Artificial Bonds

[1]S.S. Kasyap, [2*]K. Senetakis, [3]M.R. Coop, [4]J. Zhao

[1]S. S. Kasyap, Civil Engg., MTech

PhD Student

Department of Architecture and Civil Engineering

City University of Hong Kong, Hong Kong SAR

Email: ssarvadev2-c@my.cityu.edu.hk

[2]K. Senetakis, Civil Engg., MSc, PhD

Associate Professor,

Department of Architecture and Civil Engineering

City University of Hong Kong, Hong Kong SAR

Email: ksenetak@cityu.edu.hk

*Corresponding Author

[3]M. R. Coop, Civil Engg., MSc, PhD

Professor,

Department of Civil, Environmental and Geomatic Engineering

University College of London, London.

Email: m.coop@ucl.ac.uk

[4]J. Zhao, Civil Engg., MSc, PhD

Professor,

Department of Civil and Environmental Engineering

Hong Kong University of Science and Technology, Hong Kong SAR

Email: jzhao@ust.hk

Abbrevations and Notations

LBS	Leighton Buzzard sand	**OPC**	Ordinary Portland Cement
PP	Plaster of Paris	**LBOC**	LBS bonded with OPC
LBPP	LBS bonded with PP	S_q	Surface Roughness
F_N	Normal Load	F_T	Tangential Load
$F_{T,PK}$	Peak Tangential Load	$F_{T,SS}$	Steady-State Tangential Load
D_T	Tangential Displacement	η	Load Ratio
NCDT	Non-Contact Displacement Transducer	K_T	Tangential Stiffness
$K_{T,0}$	Tangnetial Stiffness at zero displacement	φ	Friction Angle
D_{cyc}	Displacement amplitude for cyclic shearing	**c**	Cohesion

Abstract

The shearing behaviour of reproduced flat LBS grains artificially bonded with ordinary Portland cement (OPC) and Plaster of Paris (PP) was examined using micromechanical experiments. Monotonic shearing tests showed a distinct variation in the load-displacement relationship at low, medium and high normal loads and a non-linear shear strength envelope was proposed. For OPC bonded sand grains, a brittle-ductile transition at 20-30 N normal load was observed and three breakage mechanisms in shearing (chipping, shear cracks, and crushing) were distinguished in accordance with the changes in the load-displacement curves. OPC bonded sands showed a predominant dilation at lower normal loads, whereas PP bonded sands were highly compressive. Based on previously published works using element-scale tests, a new mechanism for dilation under micromechanical testing was proposed in the study. Cyclic shearing tests were conducted on OPC bonded sands and the effects of increased displacement amplitude and normal load were highlighted.

Keywords: artificial bonding; cemented sands; micromechanics; non-linear strength, dilation.

1. Introduction

Bonding of granular materials either natural, due to precipitation of iron oxide, calcite or silica (Mitchell and Soga, 2005; Santamarina et al., 2001), or artificial, for example for soil improvement purposes (Saxena and Lastrico, 1978; Clough et al., 1979; Acar and El-Tahir, 1986), alters significantly the mechanical behaviour of the soil matrix. The mechanical behaviour of these bonded grains is influenced by their physical properties, irrespective of being bonded naturally or artificially (Leroueil and Vaughan, 1990). Leroueil and Vaughan (1990) also classified cemented sands and weak rocks under the same group of "structured soils". In cemented granular materials, various micro mechanisms such as cement disaggregation and fragment rearrangement are triggered by relatively small in magnitude volume changes of the grain-bond system which lead to significant changes in the response of cemented granular materials and their behaviour is set between classical soil mechanics and rock mechanics (Das et al. 2013). Many researchers have conducted laboratory experiments by means of element-scale tests on artificially cemented soils as for example in the studies by Clough et al. (1981), Lade and Overton (1989), Coop and Atkinson (1993), Haeri et al. (2005, 2006), Consoli et al. (2007), Alvarado et al. (2012), Rios et al. (2014) and Cui et al. (2017). The key parameters commonly taken into consideration in element-scale tests are the cement type and content, the confining pressure, the porosity of the sample, the stress-strain history and strain level, which collectively determine the strength, breakage mode and yielding of cemented sands.

The variation of peak stress ratio with confining stress for cemented sands is nonlinear i.e., peak stress ratio increases with decreasing rate (Lade and Overton, 1989, Chang and Kabir, 1994) and many researchers proposed non-linear strength envelope models for both cemented and uncemented soils and also jointed and intact rocks (Mogi, 1966, Barton 1976, Hoek and Brown, 1980, 1988, Barton, 2016, Wu et al., 2017, Tian et al., 2018, Shen et al., 2018). It has been shown in the literature that the classical Mohr-Coulomb failure criterion does not fit well with the failure envelopes of cemented sands which are in general non-linear in shape. Shen et al. (2018) proposed a new approximate nonlinear

Mohr-Coulomb shear strength criterion for intact rocks. This approximation provides a piecewise nonlinear envelope considering internal friction angle and cohesion parameters which are dependent on factors such as the level of confinement imposed and the unconfined compressive strength (UCS) of the material. Also, Shen et al. (2018) compared their new model with the classical Hoek-Brown (H-B) criterion and stated that the H-B criterion overestimates the stresses at higher confinements, particularly for intact rocks.

The failure mode changes from brittle to ductile as the confining stresses increase (Chang and Kabir, 1994; Schnaid et al., 2001; Wong and Baud, 2012) and a transition from brittle to ductile nature can be distinctly defined. Also, the dilation tendency i.e. the stimulus of the cemented materials under low confining pressures to increase in volume, makes their mechanical behaviour rather complex. Laboratory experiments have demonstrated that the presence of cementation or bonding decreases the dilation tendency of cemented materials (Anagnostopoulos et al., 1991; Schnaid et al., 2001; Lo et al., 2003) and that the volumetric behaviour of uncemented and cemented granular materials is different based on the shearing stage. The volumetric behaviour of uncemented sands i.e., their tendency in dilation or compression, is dependent on the initial state of the soil which is expressed by the combination of the current void ratio and magnitude of confining effective stress (Taylor, 1948; Bolton, 1986). With low effective confining pressures, the post-peak softening of uncemented dense sands is associated with dilation (i.e., increase in volume) (Lade and Yamamuro, 1996), while, in cemented sands, the dilative behaviour is initially suppressed by the bonding (Lo et al., 2003) and when the shearing reaches failure (i.e., breakage of bond), the dilation is higher and mobilizes additional shear strength (Lade and Overton, 1989).

There have been extensive numerical studies using the discrete element method (DEM) to investigate various aspects of bonded materials, including strength, bond breakage, brittle-ductile transitions, and the influences of bond thickness and confining pressure. These works have revealed the evidenced influence of the particle-scale mechanisms occurring at the contacts of the bonded grains on the bulk

behaviour of the material (e.g., Wang and Leung, 2008a, 2008b; Cheung et al., 2013; Chiu et al., 2015; Shi et al., 2015, Duan et al., 2017). Li et al. (2017) compared both experimental and 3-dimensional DEM simulation results under triaxial shearing aiming to investigate the effects of different bond strengths on the breakage mechanism of artificially cemented sands. That study highlighted the formation of shear bands due to local weakness in the sample and the consequent volumetric changes. de Bono et al. (2015) conducted DEM simulations on both cemented and uncemented materials using parallel bonds and stated that the cementation increased the brittleness of the numerical samples, while the increase of the confining pressure decreased the influence of the cementation. Wang and Leung (2008a, 2008b) highlighted the importance of bond breakage and the dilatancy of cemented materials in their mechanical response by comparing the behaviour between ordinary Portland cement and gypsum bonded sand (strong and weak bond, respectively) using parallel and series bonds. Using a biconcave bond model, Chiu et al. (2015) provided new insights in linking micro-scale and macro-scale properties of cemented soils. They found that the shape of the bond layer and its thickness are very critical in the stiffness of the bond.

There are, however, rather limited published works performing micromechanical-based experiments on bonded/cemented soils in the literature. An early study by Jiang et al. (2012) reported on the response of aluminium alloy rods bonded with epoxy adhesive under combined normal force, shear force and moment, with a primary focus on examining the differences in the mechanical behaviour between thick and thin bonds. Jiang et al. (2015) further extended the work to three dimensional contacts using aluminium hemispheres with elastic properties matching that of quartz sand. These hemispheres were bonded with epoxy adhesive. The effect of normal force on the peak strengths in shearing, bending and torsional modes was highlighted. Using sand grains bonded with gypsum plaster, Wang et al. (2017) highlighted the cemented particle crushing behaviour by defining different modes of failure. Wang et al. (2019) conducted complex loading tests by imposing shearing and combined shearing and bending loads on bonded grains at 50N normal load. These studies indicated

137 that bond thickness and the morphology of the grains at the boundary with the bonding material are

138 key factors which influence the strength parameters and mechanical behaviour of the specimens.

139 In the present study, sand grains of very low curvature (or nominally flat grains) were artificially

140 bonded using ordinary Portland cement (OPC) and Plaster of Paris (PP) representing strong and weak

141 bonds, respectively, and were further tested under monotonic shearing for a wide range of normal

142 loads. Cyclic shearing tests were also conducted on these specimens at representative normal loads.

143 The experiments were performed using a newly developed micromechanical loading apparatus for

144 cemented grains, which provides high precision of force and displacement increment and so the

145 quantification of contact stiffness of cemented grains is feasible, overcoming a limitation of the

146 apparatus previously developed by Wang et al. (2019).

147

148 **2. Description of Materials and Sample Preparation**

149 Leighton Buzzard sand (LBS) grains used in the study have sub-rounded to rounded shape and yellow

150 to brown colour. These are typical quartz type grains and were extensively tested in micromechanical

151 experiments published in the literature (Senetakis et al., 2013; Wang and Coop, 2016; Sandeep and

152 Senetakis, 2018; Nardelli and Coop, 2019). The surfaces of these LBS grains were manually flattened

153 using a stainless-steel file which produced very low local curvature and rough profiles and the grains

154 were bonded in pairs using different cementing agents. The average surface roughness (S_q) of these

155 flat LBS grains was measured for an area of 20μmx20μm and it was found to be equal to 1400μm

156 with a standard deviation of ±200μm. A typical microscopic image and a surface profile of the flat

157 surface of LBS grains used in the study are shown in Figure 1(a)-(b). The S_q values are calculated as

158 the root mean square of deviations of the asperities height with respect to the average (reference)

159 height in the considered area. Such measurements are conducted at 10 different locations for a given

160 specimen, from a set of 10 different specimens making a dataset of around 100 different measurements.

161 Two types of cementing agents, which were commercially supplied, were used for bonding the LBS

162 surfaces including Ordinary Portland Cement (OPC) and Plaster of Paris (PP), which would simulate

163 strong and weak bonds, respectively. A cement to water ratio of 0.4 was used for OPC and 0.5 for PL

164 to obtain optimum strength and these pastes were placed on the bottom flat LBS. Thereafter the top

165 LBS surface was placed on the cementing agent and subsequently the grain-cement system (specimen)

166 was allowed to bond naturally. The process was carefully monitored with a digital micro-camera so

167 that to maintain a thickness of the bond in the range of 0.6 to 0.8mm and the top grain was adjusted

168 for axial alignment within the initial setting time of the cement mortar (less than 30min). The area of

169 contact was maintained around 6 to 7.5mm^2 with a rectangular cross-section, measured using image

170 analysis, and any specimens beyond that range were discarded. Once the grains and bonding material

171 were set (initial setting time of 30min for OPC and 10min for PP), the OPC bonded specimens were

172 cured by immersion in water for 24±2hrs to attain full 1-day strength of cement mortar, while the PP

173 bonded specimens were only air dried at a temperature of 25^{0}C for 48±2hrs. Thus, the system of LBS-

174 Portland cement (denoted as LBOC) represented strong and hard bonded specimens and the system

175 LBS-Plaster of Paris (denoted as LBPP) represented weak and soft bonded specimens.

176 Figure 1(c)-(d) shows the spectrum of elements from enery dispersive X-ray spectroscopy (EDS)

177 analysis of representative samples from the OPC and PP bonds indicating the elements present in both

178 the materials along with scanning electron microscope (SEM) images. These analyses were conducted

179 after the curing/drying period of OPC and PP. PP bonding agent had Calcium (Ca) and Oxygen (O) as

180 the primary elements with traces of Sulphur (S), Magnesium (Mg) and various other compounds. OPC

181 bonding agent had a similar composition as the PP bonding agent, with Calcium and Oxygen

182 dominance with additional small amount of Silicon (Si). Unlike the EDS test results, the SEM images

183 (inset of Figure 1(c)-(d)) showed different grain shape and size for OPC and PP materials. PP particles

184 were flaky and had clay like structures with varied sizes, whereas, OPC had angular particles and silt

185   like structures, and their particle size was larger than PP. OPC showed clusters of particles bonded

186   with matrix whereas PP had a uniformly distributed matrix of particles.

187   **3. Apparatus and Testing Program**

188   A new micromechanical apparatus for investigating the behaviour of artificially bonded sand-sized

189   grains under normal, shear and bending loads was developed by Wang et al. (2019) at City University

190   of Hong Kong. The apparatus has two loading systems in the vertical and horizontal directions with a

191   linear stepping motor and a load cell in each direction. Based on these preliminary results and the built

192   of the apparatus by Wang et al. (2019), significant modifications were required, in terms of mechanical

193   arrangement of the apparatus and the testing methodology so that the upgraded apparatus can provide

194   adequate precision of forces and displacements in order to obtain high quality data in terms of force-

195   displacement relationship and subsequently contact stiffness of the bonded specimens.

196   The frame of the apparatus was stiffened with four columns with additional brace reinforcement. The

197   effective height of the apparatus was decreased considerably by shortening the connectors at various

198   stages of the loading systems in the horizontal and vertical directions. Linear bearings were used with

199   stiffener plates to guide both the horizontal and vertical motion of the system without any sway and

200   the restraint of the loading system was improved in each direction. Linear variable differential

201   transformers (LVDTs) were replaced by non-contact displacement transducers (NCDTs) and this

202   further supported measurements of high-precision displacements which are required for calculating

203   contact stiffness. In the upgraded apparatus, a stainless-steel screw shank with lower slenderness ratio

204   was used as the loading arm with one end being fixed to the load cell with a linear bearing and the

205   other end being connected to the L-mould using a screw, making it a monolithic structure between the

206   linear actuator and the L-mould. Such an upgrade to the loading arm was needed to increase the

207   stiffness of the apparatus and also to enable the apparatus to carry out cyclic shearing tests. In the

208   previous version of the apparatus by Wang et al. (2019), the loading arm was very long (~10mm)

209 which might induce additional flexibility during shearing. Shortening the loading arm and fixing it at

210 both ends increased the tangential stiffness of the apparatus. Also, the loading arm was not connected

211 to the L-moulds in the previous version. A special frame fixed to the base of the apparatus was used

212 to hold the sensors stationery and the target for the sensors was fixed to the moving loading arm. The

213 bottom L-shaped mount was fixed to a stainless-steel platform which helped to avoid unwanted

214 movements of the moulds that could disturb the testing process. The upgraded apparatus developed in

215 the present study is schematically illustrated in Figure 2. The current upgraded version of the apparatus

216 allows the study of combined normal load – shearing, without bending forces, so that at a fundamental

217 level, the interaction of these two forces can be examined. Slight modifications of the apparatus can

218 accommodate further application of combined normal – shear – bending forces on the bonded

219 specimens.

220 The load cells used in the apparatus have a capacity of 1000N with a factory repeatability of 0.05%

221 FSO (Full Scale Output) which was further improved after using high quality signal amplifiers,

222 analogue filters and data logger. The environmental and electrical noise recorded by the load cells is

223 around ±0.025N i.e. ~0.003% FSO, which provides results with adequate quality for the range of loads

224 required for tests on bonded grains. Similarly, the environmental and electrical noise of four NCDTs

225 (Non-Contact Displacement Transducers) i.e. two displacement sensors in both the vertical and

226 horizontal directions was also measured. The average value of NCDT noise varied with a maximum

227 noise of around ±0.1µm in both directions.

228 The test specimens were glued to the top and bottom mounts of the apparatus using a super glue and

229 they were allowed to dry completely; after the grains were set in position, a nominal normal load was

230 applied to ensure firm contact. Then, the vertical stepper motor was moved downwards to apply the

231 required normal load. Once the normal load was reached, the shearing was applied by horizontally

232 pushing the top L-mould and consequently the top grain moved relative to the fixed bottom grain,

233 applying in this way shearing to the specimen. In monotonic shearing tests, OPC bonded grains were

234 sheared under constant normal loads ranging from 0 to 100N for about 300μm and PP bonded grains

235 were sheared for about 200μm under constant normal loads ranging from 0 to 60N, so that the effect

236 of confinement on different strength parameters of the bonded grains could be explored. Cyclic

237 shearing tests were also conducted on OPC bonded grains at 25N and 50N constant normal load at

238 different displacement amplitudes. Table 1 provides a summary of the tests.

239 **4. Results and Discussions**

240 **4.1 Monotonic Shearing**

241 **4.1.1 Tangential Load-Displacement Behaviour**

242 Monotonic shearing tests on LBOC samples were conducted in a wide range of normal loads from 0

243 N to 100 N. The shearing tests at zero normal load (without confinement) indicate the cohesion of the

244 specimens. The shear forces developed in zero normal load tests are due to the combined effect of

245 cohesion and roughness between the bounding surface and the bonding agent (Tian et al., 2018). Figure

246 3(a)-(b) shows the tangential load – displacement behaviour of both LBOC and LBPP specimens at

247 zero normal load. The LBOC specimens showed a peak tangential load ($F_{T,PK}$) of around 5.6N and a

248 steady state tangential load ($F_{T,SS}$) of around 1.85N, while, the LBPP specimens showed lower values

249 than LBOC specimens with $F_{T,PK}$ of 1.44 N and $F_{T,SS}$ of 0.62 N. The softening behaviour or the post-

250 peak force reduction indicated a force-drop (F_d) of around 57% and 67% for LBPP and LBOC

251 specimens, respectively.

252 Based on the variation of the tangential load – displacement curves, the tests on LBOC specimens

253 were divided into two classes as (i) low – medium range (0 N to 30 N) and (ii) medium – high range

254 (40 N to 100 N). This distinction of the tests was based on the linear and non-linear nature of the initial

255 part of the tangential load – displacement curves (or tangential stiffness variation), the formation of

256 post-peak force reduction, the volumetric behaviour and, the brittle-ductile transition zone. Few of

257 these parameters are interlinked and the details are explained in the subsequent discussions. A limited

258 set of monotonic shearing tests on LBPP specimens was carried out at normal loads ranging from 0 N

259 to 60 N and it was not feasible to make a distinction of the tangential load-displacement curves similar

260 to LBOC. However, an apparent classification was made into low-medium and medium-high normal

261 load cases (8N to 25N and 25N to 60N, respectively) based on the non-linearity of the tangential load-

262 displacement curves.

263 Figure 3(c)-(d) shows the tangential load – displacement curves for the low-medium normal load range

264 for LBOC and LBPP specimens, respectively. A very stiff and almost linear increase in the tangential

265 load up to the peak and then a post-peak force reduction occurred for LBOC specimens but a minor

266 post-peak reduction occurred only at 8N normal load for LBPP. At other normal loads in the low-

267 medium range of LBPP specimens, the tangential load-displacement behaviour was elasto-plastic with

268 a gradual shift into a steady-state regime. Similar to the zero normal load tests in the previous section,

269 a smooth trend was observed before the steady state and then a rough profile occurred. As the normal

270 loads increased to the medium-high range, the tangential load-displacement curves became non-linear

271 with hardening behaviour for both LBOC and LBPP specimens and the corresponding curves are

272 shown in Figure 3(e)-(f), respectively. Occasional stick-slip instability was observed for LBOC

273 specimens while all the curves for both the specimens showed a rough profile indicating a dominance

274 of friction mechanism over cohesion. Also, the tangential loads mobilized in strong LBOC specimens

275 were higher than the soft LBPP specimens.

276 **4.1.2 Tangential Load-Normal Load Variation**

277 The governing factors for the post-peak softening behaviour under low confining pressures for

278 element-scale tests have been mentioned to be the breakage of the cement bridges at lower confinement

279 and the grain crushing and pore collapse at higher confinement (Menendez et al., 1996; Das et al.,

280 2013). This behaviour can also be correlated to the brittle and ductile failures of the specimens and a

281 distinct transition between the two failure modes (brittle-ductile transition); this problem has been well

282   studied using laboratory element-scale experiments, specifically for bonded grains and rocks (Byerlee,

283   1968; Coop and Atkinson, 1993; Chang and Kabir, 1994; Coop and Wilson, 2003; Wong and Baud,

284   2012). The phenomenon of brittle-ductile transition can be understood from the strength envelopes

285   and the associated failure mechanisms observed in the specimens. Figure 4 shows the variation of the

286   peak tangential load ($F_{T,PK}$) with normal load (F_N) for LBOC and LBPP specimens. For LBOC

287   specimens, the $F_{T,PK}$ values increased with normal load, but at a decreasing rate and a polynomial

288   trendline (dashed lines in Figure 4) could fit the data with a resultant coefficient of correlation of 0.97

289   for LBOC test results, and 0.99 for LBPP test results.

290   To further understand the physical meaning of the variation of $F_{T,PK}$ with normal load, a bilinear

291   trendline (P-Q-R in Figure 4a) was fitted to the datapoints which was optimized for the highest R^2

292   values, for LBOC specimens. The datapoints at low-medium normal loads were fitted with R^2 of 0.95

293   and the datapoints at medium-high normal loads were fitted with R^2 of 0.87. This bilinear fitting helped

294   to differentiate the brittle, ductile and the transition zones as indicated in Figure 4(a). The shaded part

295   in this figure, i.e., F_N = 20 to 30 N, indicates the brittle-ductile transition for the current state of the

296   LBOC specimens, which would change with bond type and bond thickness. For LBPP specimens, the

297   bilinear trend could not be distinguished to define a brittle-ductile transition. The proposed range of

298   normal loads for brittle-ductile transition in LBOC specimens is substantiated also with the load ratio

299   (η = $F_{T,PK}/F_N$) variation as shown in Figure 4(a) on the secondary vertical axis. The datapoints of η

300   were fitted with a power function and the trend of this curve started with η = 3 at 2.5 N normal load

301   and reached a saturation level of around 0.5 to 0.6 (53% decrease) beyond the proposed brittle-ductile

302   transition. On the other hand, LBPP specimens showed a 33% decrease in η (0.56 to 0.4) over the

303   considered normal load range and a power function fitting this data indicated a load ratio saturating at

304   around 0.35.

305   The variation of peak tangential load with normal load data shown in Figure 4 has a nonlinear trend

306   and the data within the given normal load range was fitted using an expression as shown in Eq.(1).

307   This equation was developed based on the framework of Hoek-Brown empirical model for rock

308   samples, translated in terms of loads. Eq.(1) depends on the cohesion (C_0) and crushing load (F_C) of

309   the specimens, resulting in tangential load (F_T) at a given normal load (F_N). The coefficient α in these

310   expressions is obtained from Eq.(2) using the F_C value of the given specimen type (LBPP or LBOC).

311    $$F_T = C_0 \left\{ \frac{\alpha\, F_N}{F_C} + 1 \right\}^{0.7}$$ Eq.(1)

312    $$\alpha = 107.4 - 0.42 * F_C$$ Eq.(2)

313   Appendix-1 explains the details of the crushing test results. Figure 4(c) shows the fitting of the

314   experimental data with the empirical nonlinear envelope for bonded specimens and the corresponding

315   R^2 values are also shown in this figure. In Eq.(1), the empirical parameters α and the exponent 0.7 are

316   highly dependent on the crushing loads of the current specimen type, and these both parameters can

317   be understood to be mutually dependent. The trend of strength envelope was with increasing

318   magnitude at decreasing rate, and this suggests that the exponent of the equation must be less than 1.

319   The α value becomes unstable as the crushing strength values increase and hence extra considerations

320   might be required in both α values and the exponent for different specimens with greater crushing

321   strengths.

322   **4.1.3 Tangential Stiffness Behaviour**

323   The tangential stiffness (K_T) at a given tangential displacement was obtained by numerical

324   differentiation of the tangential load-displacment datapoints. The degradation of tangential stiffness

325   with displacement is highlighted to understand the non-linearity of the F_T-D_T curves. For LBOC

326   specimens, two classes of stiffness degradation curves were identified based on the applied normal

327   load magnitude, as shown in Figure 5(a)-(b). In the low – medium normal load range, the stiffness

328   degradation curves were almost horizontal (compared to the extent of degradation in other test cases)

329   for a certain range of tangential displacement and then the curves dropped suddenly to zero stiffness.

13

330 In the medium – high normal load range, the stiffness degradation curves were highly non-linear from

331 early stages of the measured displacements. The stiffness degradation curves in both the classes of

332 normal loads showed a few inconsistencies due to the chipping of the bonding material and early

333 damages occurred in the specimen. However, within the scatter of the data, it was observed that the

334 maximum tangential stiffness values (or initial tangential stiffness, $K_{T,0}$; tangential stiffness value

335 defined at the lowest resolvable tangential displacements) was higher at lower normal loads. Hamidi

336 and Haeri (2008) stated that the tangential stiffness of bonded sands becomes close to that of sands

337 without bonds at higher confinements. The $K_{T,0}$ value at $F_N = 8N$ was around 1500N/mm and at $F_N =$

338 90N, the value was around 2000N/mm. In the medium range of normal loads, the initial tangential

339 stiffness values increased as high as 10000N/mm at around $F_N = 20N-25N$.

340 The tangential stiffness degradation curves for LBPP specimens did not show such distinction in shape

341 based on the normal load. However, with an increase in normal load the stiffness values decreased and

342 all the curves showed a nonlinear decrease in K_T with tangential displacement. The values of K_T for

343 LBPP specimens were around 2 to 3 times lower than that of LBOC specimens. The stiffness

344 degradation curves for LBPP specimens are shown in Figure 5(c)-(d).

4.2 Cyclic Shearing: LBOC Specimens

346 Cyclic shearing tests of five cycles were conducted on LBOC specimens with displacement amplitude

347 (D_{cyc}) of 10 µm and 25 µm at 25 N normal load and, with D_{cyc} of 10 µm at 50 N normal load. These

348 tests give insights into the cyclic shearing behaviour of LBOC specimens at different combinations of

349 normal loads and displacement amplitudes. Figure 6(a)-(b) compares the first cycles of tangential load

350 – displacement curves at different $F_N – D_{cyc}$ combinations. Only the 25 N–25 µm test reached steady-

351 state and had considerable plastic displacements and energy dissipation in shearing. The 25 N–10 µm

352 test was unloaded at peak load and hence a smaller amount of plastic displacements was observed

353   while in the case of 50 N–10 µm test, the maximum tangential load reached was prior to the occurrence

354   of the peak load resulting in predominantly elastic behaviour with much lesser energy dissipation.

355   In Figure 6(a), the 25N–25µm test showed higher value of maximum tangential load ($F_{T,max}$) in the

356   unloading phase, whereas the $F_{T,max}$ value in the loading phase was the same as in the 25N–10µm test.

357   This can be explained from the volumetric behaviour of the specimen in the loading and unloading

358   phases. Figure 6(c) shows the variation of δ_N with δ_T, where the curve shows dilation in the unloading

359   phase (backward shear) and compression in the loading/reloading phase (forward shear). The fracture

360   developed in the bonding of the specimen closes while unloading (backward shear) and the blocks of

361   the bonding material on either sides of fracture tend to slide against each other. The generated dilation

362   and frictional behaviour in the specimen (Video S1) leads to the excess mobilization of tangential

363   loads as shown in the Figure 6(a). In the reloading phase, the crack opens and might only progate the

364   already existing crack, leading to peak tangential load similar to that of the 25N–10µm test. This

365   phenomenon continues through the five cycles of shearing with decreasing amplitudes of dilation and

366   compression as shown in Figure 6(c). Figure 7(a)-(c) shows the five cycles of hysteretic loops for the

367   three classes of tests. For 10µm tests, the hysteretic loops showed no significant plastic deformations

368   and hence the secant stiffness (slope of hysteresis) can be considerable. For the 25N–25µm test, the

369   elastic stiffness can be approximated from the slope of loading and unloading parts of the curves as

370   indicated in Figure 7(c).

371   The dissipated energy is generally an indicator of the frictional losses in the contact of two bodies and

372   is calculated from the area of the closed loop in a cyclic loading process. In the case of bonded grains,

373   the adhesive forces also compensate for the energy losses in cyclic shearing. These losses include the

374   elastic or plastic nature of opening and closure of microcracks in the process of cyclic loading. The

375   difference of dissipated energy (ΔE) values in the three test cases, as shown in Figure 7, is more than

376   one order of magnitude. The trend of dissipated energy is similar to the trend of slope of hysteresis

377   with the 25 N–25 µm case dissipating the maximum and the 50 N–10 µm case dissipating the

minimum. However, there were observed differences with increasing number of cycles within each

test case and this variation is shown in Figure 8(a). Bar graphs in this figure indicate the ratio of the

dissipated energy in each cycle to the first cycle of shearing and their numerical values are shown in

Table 2. At a given normal load of 25N, the two displacement amplitude cases showed significant

differences in the dissipated energy values. In cycle 1 of shearing, the dissipated energy for 25N-10μm

case was around 0.16N-mm while the 25N-25μm case had a corresponding value of 1.12N-mm, which

is around 7 times higher than the former case. With 10μm of D_{cyc}, the curves are still in the elastic

region of behaviour and hence the values of dissipated energy are smaller than the 25μm case where

the curves entered the plastic deformation stage. Also with the number of shearing cycles the trend

was different for lower and higher displacement amplitudes. With 10μm of D_{cyc}, at both 25N and 50N

normal load, the ΔE values increased by around 1.3 times (30% increase) from cycle 1 to cycle 5,

which can be understood as increased frictional losses incurred by the damage of the bonding agent

(discussed later in this section). On the other hand, with 25μm of D_{cyc}, the ΔE values decreased by

around 0.1 times (10% decrease) from cycle 1 to cycle 5, as the specimens are well within the elastic

region and so no damage was propagated with the increase in shearing cycles.

The hysteretic damping ratio values are calculated based on the elastic energy stored in each cycle and

the variation for three test cases and five cycles of loading are shown in Figure 8b. The damping ratio

values are also shown in Table 2. The variation of damping ratio was similar to the variation of

dissipated energy values as shown in Figure 8a and Table 2 with 25N-25μm case showing the

maximum damping due to the induced plastic deformations.

From one cycle to another, the slope of hysteresis showed a decreasing trend, but the variation was

smaller in all the test cases. As the loading cycles increased, micro cracks in the cemented specimens

were generated and this decreased the load carrying capacity (combined stiffness in loading and

unloading) of the specimens. The tangential load amplitude ($F_{T,Amp}$) is the summation of the maximum

402   tangential loads attained in loading and unloading phases of each cycle. The variation of $F_{T,Amp}$ is

403   shown in Figure 8(b) with bar graphs. The 25 N–25 µm test showed the maximum value and the 50

404   N–10 µm test showed the least. This is expected since the 50 N–10 µm test did not reach its peak load

405   in the loading phase, and thus it remained in a relatively elastic state unlike the 25 N normal load test.

406   Also, the attenuation of $F_{T,Amp}$ with increasing cycles was higher for the cases where ductile behaviour

407   was the dominant, i.e., at 25 N normal load. The 25 N–10 µm and 25 N–25 µm tests showed an

408   attenuation of 10% to 13% of $F_{T,Amp}$. The consequences of this damage were explained in terms of

409   energy dissipation using Figure 8a. Also, the tangential load values reflect the damage developed in

410   the bonding agent. During the first cycle of shearing under 25N-25µm case, the $F_{T,Amp}$ value was

411   highest at 47.8N where the major damage (or shear crack) was observed. In the consecutive cycles,

412   lower $F_{T,Amp}$ values (~43.5N) were recorded as either the existing crack/damage was propagating or

413   new cracks (only minor) were developing during shearing.

414   After the first cycle of tangential loading and unloading, a macroscopic failure was observed in the 25

415   N–25 µm test (Video S1). Opening and closure of the crack(s) allowed the specimen to dissipate the

416   energy through this process, leading to a maximum energy dissipation and tangential load amplitude

417   and, a minimum hysteresis slope. In other tests at lower displacement amplitude (10 µm), no visible

418   cracks/failure were observed. However, decreasing stiffness and tangential load amplitude imply that

419   some microcracks were developed in the cementation of the specimens. With the number of shearing

420   cycles, the damage was induced in the cementation by either propagation of microcracks and/or

421   formation of new microscopic cracks.

422   **4.3 Dilatancy and Breakage Mechanisms**

423   **4.3.1. Influence of normal load on dilatancy**

424   After Rowe (1962) and Rowe et al. (1963), the relation between stress and dilatancy for cemented

425   sands has been studied extensively in the literature (Coop and Atkinson, 1993; Cuccovillo and Coop,

426   1999; Schnaid et al., 2001; Yu et al., 2007; Trivedi, 2010; Terzis and Laloui, 2019). The breakage

427   mechanism also depends on the magnitude of the normal load. Since the bonding is brittle, cohesion

428   dominates at lower normal loads and the specimen will have brittle breakage. At higher normal loads,

429   the cohesion between the grains becomes a less influential factor and friction carries the tangential

430   loads leading to ductile breakage of the specimen.

431   Similar to the expected macroscopic behaviour of granular materials (e.g., Atkinson, 1993, Muir

432   Wood, 2007, Cuccovillo and Coop, 1999), the present micromechanical experiments also showed

433   dilative behaviour at lower normal loads and compressive behaviour at higher normal loads for bonded

434   sand grains. The rigid loading arm for shearing is connected to a linear bearing at the farther end to

435   accommodate the vertical movements (Figure 2b) and the measurement of vertical displacements

436   during shearing is feasible. The dilative or compressive behaviour of LBOC specimens reciprocated

437   with their breakage mechanism based on the magnitude of the applied confinement.

438   Figure 9(a) shows the variation of vertical displacement i.e., dilation (-ve) or compression (+ve), with

439   shearing displacement for LBOC specimens at different normal loads. It is evident that as the

440   confinement (or normal load) increases, the behaviour is shifting from pure dilation to pure

441   compression. The tests with normal load lower than 20 N showed pure dilative behaviour with

442   maximum dilation of around 72 µm at 0 N normal load (note that the terms "dilation" and

443   "compression" are discussed in the study by means of vertical displacement with positive values

444   denoting compression). The maximum compression was around 140 µm at 100 N normal load test. At

445   the normal load range of the proposed brittle-ductile transition (i.e., 20 to 25 N), the tests showed

446   minimum change in the vertical displacement. The inset of Figure 9(a) shows the vertical displacement

447   variation for 20 N normal load case. The curve showed pure dilative behaviour in the beginning and

448   later started to show compressive behaviour. This is related to the breakage of the bonding between

449   the LBS grains as it will be discussed later in this section.

18

450   Figure 9(b) shows a representative test at $F_N = 8$ N comparing the variation of tangential load, normal

451   load and normal displacement with shearing displacement. The normal displacement curve showed a

452   dilative behaviour apart from a small initial compressive stage and the slope of the curve (rate of

453   dilation) changed at the start of the steady state. The rate of volumetric change (i.e., slope of the volume

454   change versus tangential displacement) is also maximum at a tangential displacement where the

455   corresponding tangential loads started to decrease from their peak value. Similar observation was

456   reported by Wang and Leung (2008b) from triaxial compression tests on Ottawa sand mixed with

457   cement slurry. Figure 9(c) shows the variation of the rate of dilation with tangential displacement for

458   representative tests at low, medium and high normal loads. At lower normal loads, the rate of dilation

459   was negative and was maximum during the peak load and then it tended to reduce to zero during the

460   later stages of shearing. At medium normal loads, the curves showed almost zero dilation rate until

461   breakage occurred in the cementation and then they showed compressive behaviour (i.e., positive rate

462   of dilation). The higher normal load tests showed purely compressive behaviour with a constant value

463   of positive rate of dilation.

464   **4.3.2 Breakage mechanisms**

465   Three modes of breakage were observed in the specimens (i) chipping and specimen separation (at

466   lower normal loads), (ii) shear cracks and splitting (at medium normal loads), and (iii) crushing (at

467   higher normal loads). All these three phenomena were observed only in the bonding material and the

468   sand grains showed no signs of failure. Wang et al. (2019) stated that shearing tests of LBS grains

469   bonded with gypsum plaster at $F_N = 50$N showed yielding at 21N and the failure was attributed to the

470   rotation of the whole specimen about the bottom sand particle without any visible cracks.

471   *Mode-1: Chipping and specimen separation* type of failure was observed in specimens sheared at

472   lower normal loads ($F_N < 20$N). Figure 10(a) shows the three stages of a specimen sheared at $F_N = 8$

473   N i.e., the initial stage after the application of normal load, chipping during shearing and clean

474   separation of specimen after the removal of the normal load. The high dilatancy at low normal loads

475   in the current set of specimens indicated the mechanism of failure and energy dissipation. During

476   shearing, the specimens with low confinement tended to dissipate energy by bond splitting rather than

477   shearing along the bond (weakest link in the specimens). In the process of bond splitting/specimen

478   separation, the specimens showed significant dilation while shearing due to uplift tendency (i.e.,

479   termed as dilation) of the top grain. At the interface of the bonding material and the grain, a slight

480   chipping was observed while shearing and this is shown in Video S2. Once the complete separation

481   occurred, the dilation rate reached zero and the friction became the dominant mechanism of shear

482   strength, overtaking cohesion and dilation counterparts.

483   *Mode-2: Shear cracks and splitting* type of failure was observed in specimens sheared at the medium

484   range of normal loads ($F_N = 20\ N – 30\ N$). Video S3 shows the failure of a specimen with shear cracks

485   and splitting occurring in the bonding material. These are only the visible failures observed in the

486   specimens, but many microscopic cracks are expected in the sample which would lead to the failure

487   of the specimen. This type of failure is a special case since the normal load pertaining to this class was

488   proposed to be brittle-ductile transition in the previous sections. In these specimens, the dilation rate

489   was almost zero and the shear cracks in the specimen showed a distinctive phenomenon in the

490   tangential load – displacement curves. Figure S1 shows the tangential load – displacement curves at

491   20 N and 25 N normal loads. During the peak tangential load, no cracks were visible in the specimen

492   but during the steady state shearing the cracks started to expand and later a sudden drop in tangential

493   load was observed (as indicated in Figure S1). This is the point where the specimen started to show

494   compressive behaviour from zero dilation condition as indicated in the subset of Figure 9(a). These

495   shear cracks were always inclined in the direction of shearing at an angle of 50° to 60° with respect to

496   the horizontal.

497   *Mode-3: Crushing* type of failure was observed in the specimens sheared at higher normal loads (F_N

498     $> 50\ N$). Crushing was observed only in the bonding material and the crushing behaviour of the

499   specimens at 90 N is shown in Video S4. At this high normal load, the stresses created in the specimen

500   are almost nearing to one-day crushing strength of cement mortar and due to the imposition of shearing

501   the bonding material loses its strength to resist. In this stage, the specimens showed pure compression

502   in the normal displacement against tangential displacement curves. However, the crushing failure

503   mechanism was not reflected in the tangential load – displacement curves as in the shear cracks mode,

504   except for the delayed stiffness degradation and highly nonlinear curves.

505   The LBPP specimens showed purely compressive behaviour except for zero normal load shearing.

506   Figure 9(d) shows the variation of normal displacement with shearing displacement at different normal

507   loads. The damage occurred on the specimens was crushing type with no proper shear cracks on the

508   bonding material and the material appeared to be squeezed out from the specimen due to the soft nature

509   of the plaster. Wang and Leung (2008a) observed a similar behaviour for gypsum plaster with great

510   volumetric contraction and bulging type of failure. Figure 10(b) shows representative images of

511   specimen breakage at different normal loads for LBPP specimens.

512   Relating dilatancy with stress is a general mode of understanding the strength characteristics of both

513   uncemented and cemented soils (Taylor, 1948; Rowe, 1962; Bolton, 1986; Been and Jefferies, 2004).

514   Figure 11 shows the effects of confinement on the strength (load ratio, η) and dilatancy ($d\delta_v / d\delta_t$)

515   behaviour on LBOC specimens. At three ranges of normal loads (i.e. low, medium and high) the curves

516   showed a decreasing load ratio while the dilatancy rate was shifting from negative to positive values

517   (i.e. from dilation to compression). In all the three cases, the curves ultimately reached zero dilation

518   rate (though oscillating) but the time required to reach this condition increased at higher norma loads.

519   At lower normal loads in pure dilation, the specimen required less time to reach zero dilation rate

520   compared with the medium normal load range (based on the density of data points on the curve). At

521   higher normal loads the rate of dilation was almost constant with small fluctuations. The strength (or

522   load ratio) of bonded sands is contributed by cohesion, dilatancy and friction components (Lambe,

523   1960). Cuccovillo and Coop (1999) indicated that the energy dissipated in frictional loss and bond

breakage comprise the total work done by the stresses. The frictional loss includes the steady-state and the dilation components. However, in element-scale cemented samples, dilatancy develops under shearing after the breakage of cohesion between the grains. In the current micromechanical tests, dilatancy was observed as a consequence of breakage of the cohesion through the process of shearing as a simpler mode of energy dissipation. As the top grain is moved horizontally for shearing, the specimen tends to separate from the bonding material by breaking the bond. Since the normal load is maintained at a given constant value in a force-controlled manner, as the specimen dilates (or separates from bonding) it exerts an additional force on the loading system making the micro-stepper motors to move upwards to resume the normal load to its original values. Also, the bond does not break completely at the peak tangential load, but some bond clusters are formed (Wang and Leung, 2008b). These phenomena make the dilation to continue beyond the start of the steady-state unlike element-scale tests. However, this occurs at lower normal loads only. At higher normal loads, the top grain will be more partial to shearing along the bond and hence dilation it not observed. This mechanism of consequent bond breakage, energy dissipation and dilation is distinct for micromechanical experiments when compared to element-scale testing. Further investigation on the interaction of shear load – normal load (and perhaps shear load – normal load – bending load) would be useful taking into account different types of bonds and bond thickness.

5. Conclusions

The study presented micromechanical tests on bonded sand-size grains investigating the tangential load-displacement behaviour in monotonic and cyclic shearing, providing insights into the failure mechanisms of the specimens and proposing an empirical expression for the failure envelope of bonded grains. The experiments were performed by upgrading and stiffening an existing micromechanical apparatus providing in this way higher precision of forces and displacements so that contact stiffness can be measured reliably. The stiffness of the apparatus was improved, and non-contact displacement transducers were used for high precision measurements of displacements.

549 Reproduced flat LBS grains which represent granular material with low curvature were artificially

550 bonded with ordinary Portland cement (LBOC) and plaster of Paris (LBPP). Table 3 gives a qualitative

551 summary of the behaviour of the bonded grains from the micromechanical tests. Monotonic shearing

552 tests were conducted on these two classes of bonded grains in a wide range of normal loads. LBOC

553 specimens showed higher shear strength compared to LBPP specimens, both having a non-linear

554 strength envelope. A new empirical non-linear strength envelope was proposed in which the tangential

555 load increased with decreasing rate as the normal load increased. At lower normal loads ($F_N < 20$ N),

556 the LBOC specimens showed predominantly dilative behaviour leading to post-peak force reduction.

557 Such specimens had brittle failure with chipping and bond separation. At higher normal loads ($F_N >$

558 40 N), the LBOC specimens had compressive behaviour and the specimen failed due to crushing of

559 the bonding material. A brittle-ductile transition was proposed to be at $F_N = 20 - 25$ N based on the

560 curvature of the strength envelope, failure type and dilatant behaviour. Such distinction was not

561 observed for LBPP specimens and all the specimens showed compressive behaviour except for zero

562 normal load test. The tangential stiffness also showed decreasing trend as the normal load increased,

563 with LBOC specimen showing 2 to 3 times higher values than LBPP. The shape of stiffness

564 degradation curves was different for LBOC specimens at lower and higher normal loads following the

565 tangential load – displacement curves. Cyclic shearing tests on LBOC specimens showed higher

566 energy dissipation and lower stiffness with increased displacement amplitude at a given normal load.

567 It was observed that the energy dissipation is higher if the maximum tangential load reached in cyclic

568 shearing is equal to the peak tangential load at a given normal load and the damage is higher in such

569 cases if the displacement amplitude is also larger. An attempt was made to apply stress-dilatancy

570 theory to the current micromechanical tests on LBOC specimens. The dilatancy rate was maximum at

571 the peak tangential load and the rate reduced as the shearing continued. From the current

572 micromechanical tests, a mechanism of continuous mobilization of cohesion through shearing is

573 suggested owing to the increasing dilation after steady state sliding for bonded specimens.

574

575

Acknowledgements

582

583

584

References

Acar, Y.B., El-Tahir, A.E. 1986. Low strain dynamic properties of artificially sands, Journal of Geotechnical Engineering - ASCE, 112(11), 1001-1015.

Alvarado, G., Lui, N., Coop, M.R. 2012. Effect of fabric on the behaviour of reservoir sandstones, Canadian Geotechnical Journal, 49(9)m 1036-1051.

Anagnostopoulos, A.G., Kalteziotis, N., Tsiambaos, G.K., Kavvadas, M. 1991. Geotechnical properties of the Cornith Canal marls, Geotechnical and Geological Engineering, 9(1), 1-26.

Atkinson J., 1993. An Introduction to the Mechanics of Soils and Foundations, McGraw-Hill International Series in Civil Engineering.

Barton, N. 1976. The shear strength of rock and rock joints, International Journal of Rock Mechanics and Mining Sciences and Geomechanics Abstracts, 13(9), 255-279.

Barton, N. 2016. Non-linear shear strength for rock, rock joints, rockfill and interfaces, Innovative Infrastructure Solutions, 1(30).

Been, K., Jefferies, M. 2004. Stress-dilatancy in very loose sand, Canadian Geotechnical Journal, 41, 972-989.

Bolton, M.D. 1986. The strength and dilatancy of sands, Geotechnique 20(1), 65-78.

Byerlee, J.D. 1968. Brittle-ductile transition in rocks, Journal of Geophysical Research, 73, 4741-4750.

Chang, C.S., Kabir, M.G., 1994. Mechanics for brittle and ductile behavior of cemented sands. In: Proceedings of XIII ICSMFE, New Delhi, 369-372.

Cheung, L.Y.G, O'Sullivan, C. Coop, M.R. 2013. Discrete element method simulations of analogue reservoir sandstones, International journal of Rock Mechanics and Mining Science, 63, 93-103.

Chiu, C.C., Weng, M.C., Huang, T.H. 2015. Biconcave bond model for cemented granular material, Journal of GeoEngineering, 10(3), 91-103.

Clough, G.W., Iwabuchi, J., Rad, N.S., Kuppusamy, T. 1979. Silicate-stabilized sands, Journal of Geotechnical Engineering - ASCE, 105(1), 65-82.

Clough, G.W., Sitar, N., Bachus, R.C. 1981. Cemented sand under static loading, Journal of Geotechnical Engineering Division - ASCE, 107(6), 799-817.

Consoli, N.C., Foppa, D., Festugato, L., Heineck, K.S. 2007. Key parameters for strength control of artificially cemented soils, Journal of Geotechnical and Geoenvironmental Engineering, 133(2), 197-205.

Coop, M.R., Atkinson, J.H. 1993. The mechanics of cemented carbonate sands, Géotechnique 43(1), 53-67.

Coop, M.R., Wilson, S.M. 2003. Behaviour of hydrocarbon reservoir sands and sandstones, Journal of Geotechnical and Geoenvironmental Engineering, 129(11), 1010-1019.

Cuccovillo, T., Coop, M.R. 1999. On the mechanics of structured sands, Geotechnique, 49(6), 741-760.

Cui, M.J., Zheng, J.J., Zhang, R.J., Lai, H.J., Zhang, J. 2017. Influence of cementation level on the strength behaviour of bio-cemented sand, Acta Geotechnica, 12, 971-986.

Das, A., Tengattini, A., Nguyen, G., Einav, I. 2013. A micromechanics based model for cemented granular materials, Q. Yang et al. (Eds.): Constitutive Modeling of Geomaterials, SSGG, 527-534.

de Bono, J., McDowell, G., Wanatowski, D. 2014. Investigating the micro mechanics of cemented sand using DEM, International Journal for Numerical and Analytical Methods in Geomechanics, 39(6), 655-675.

Duan, K., Kwok, C.Y., Ma, X. 2017. DEM simulations of sandstone under true triaxial compressive tests, Acta Geotechnica, 12, 495-510.

Haeri, S.M., Hamidi, A., Hosseini, S.M., Asghari, E., Toll, D.G. 2006. Effect of cement type on the mechanical behaviour of a gravely sand, Geotechnical and Geological Engineering Journal, 24(2), 335-360.

Haeri, S.M., Hosseini, S.M., Toll, D.G., Yasrebi, S.S. 2005. The behaviour of an artificially cemented sandy gravel, Geotechnical and Geological Engineering Journal, 23(5), 537-560.

Hamidi, A., Haeri, S.M. 2008. Stiffness and deformation characteristics of a cemented gravely sand, International Journal of Civil Engineering, 6(3), 159-173.

Hoek, E., Brown, E.T. 1980. Empirical strength criterion for rock masses, Journal of Geotechnical Engineering Division - ASCE, 106(9), 1013-1025.

Hoek, E., Brown, E.T. 1988. The Hoek-Brown failure criterion – a 1988 update, In: Proceedings of the 15th Canadian rock mechanics symposium, 31-38.

Jiang, M.J., Jin, S.L., Shen, Z.F., Liu, W., Coop, M.R. 2015. Preliminary experimental study on threedimensional contact behavior of bonded granules, In: IOP Conference Series: Earth and Environmental Science, 26(1), 012007.

Jiang, M.J., Sun, Y.G., Li, L.Q., Zhu, H.H. 2012. Contact behaviour of idealized granules bonded in two different interparticle distances: An experimental investigation, Mechanics of Materials, 55, 1-15.

Lade, P.V., Overton, D.D. 1989. Cementation effects in frictional material, Journal of Geotechnical Engineering – ASCE, 115, 1373-1387.

Lade, P.V., Yamamuro, J.A. 1996. Undrained sand behaviour in axisymmetric tests at high pressures, Journal of Geotechnical Engineering – ASCE, 122(4), 309-316.

Lambe, T.W. 1960. A mechanical picture of shear strength in clay, Research Conference on Shear Strength of Cohesive Soils, University Colorado Press, Boulder, CO, 555-580.

Leroueil, S., Vaughan, P.R. 1990. The general and congruent effects of structure in natural soils and weak rocks, Geotechnique, 40(3), 467-488.

Li, Z., Wang, Y.H., Ma, C.H., Mok, C.M.B. 2017. Experimental characterization and 3d DEM simulation of bond breakages in artificially cemented sands with different bond strengths when subjected to triaxial shearing, Acta Geotechnica, 12, 987-1002.

Lo, S.C.R., Lade, P.V., Wardani, S.P.R. 2003, An experimental study of the mechanics of two weakly cemented soils, Geotechnical Testing Journal, 26(3), 328-341.

Menendez, B., Zhu, W., Wong, T.F. 1996. Micromechanics of brittle faulting and cataclastic flow in Brea sandstone, Journal of Structural Geology, 18(1), 1-16.

Mitchell, J., Soga, K. 2005. Fundamentals of Soil Behaviour, 3rd ed., John Weily and Sons.

Mogi, K. 1966. On the pressure dependence of strength of rocks and the Coulomb fracture criterion, Tectonophysics, 21(3), 273-285.

Muir Wood D., 2007. Soil Behaviour and Critical State Soil Mechanics, Cambridge University Press.

Nardelli, V., Coop, M.R. 2019. The experimental contact behaviour of natural sands: normal and tangential loading, Geotechnique, 69(8), 672-686.

Rios, S., da Fonseca, A.V., Baudet, B.A. 2014. On the shearing behaviour of an artificially cemented soil, Acta Geotechnica, 9, 215-226.

Rowe, P.W. 1962. The stress-dilatancy relation for static equilibrium of an assembly of particles in contact, Proceedings in Royal Society of London A, 269, 500-527.

Rowe, P.W., Oates, D.B., Skermer, N.A. 1963. The stress-dilatancy performance of two clays, In: Laboratory shear testing of soils, ASTM Special Technical Publications, 134-143.

Sandeep, C.S., Senetakis, K. 2018. Grain-scale mechanics of quartz sand under normal and tangential loading, Tribology International, 117, 261-271.

Santamarina, J.C., Klein, A., Fam, M.A. 2001. Soils and waves: Particulate material behaviour, characterization and process monitoring, Journal of Soils and Sediments, 1(2).

Saxena, S.K., Lastrico, R.M. 1978. Static properties of lightly cemented sand, Journal of Geotechnical Engineering Division - ASCE, 4(12), 1449-1464.

Schnaid, F., Prietto, P.D.M., Consoli, N.C. 2001, Characterization of cemented sand in triaxial compression, Journal of Geotechnical and Geoenvironmental Engineering, 127(10), 857-868.

Senetakis, K., Coop, M.R., Todisco, M.C. 2013. Tangential load-deflection behaviour at the contact of soil particles, Geotechnique Letters, 3(2), 59-66.

Shen, B., Shi, J., Barton, N. 2018. An approximate nonlinear modified Mohr-Coulomb shear strength criterion with critical state for intact rocks, Journal of Rock Mechanics and Geotechnical Engineering, 10, 645-652.

Shi, Z., Jiang, T., Jiang, M., Liu, F., Zhang, N. 2015. DEM investigation of weathered rocks using a novel bond contact model, Journal of Rock Mechanics and Geotechnical Engineering, 7, 327-336.

Taylor. 1948. Fundamentals of Soil Mechanics, New York: Wiley.

Terzis, D., Laloui, L. 2019. Cell-free soil bio-cementation with strength, dilatancy and fabric characterization, Acta Geotechnica, 14, 639-656.

Tian, Y., Liu, Q., Ma, H., Liu, Q., Deng, P. 2018. New peak shear strength model for cement filled rock joints, Engineering Geology, 233, 269-280.

Trivedi, A. 2010. Strength and dilatancy of jointed rocks with granular fill, Acta Geotechnica, 5, 15-31.

Wang, W., Coop, M.R. 2016. An investigation of breakage behaviour of single sand particles using a high-speed microscope camera, Geotechnique, 66(12), 984-998.

Wang, W., Coop, M.R., Senetakis, K. 2019. The Development of a Micromechanical Apparatus Applying Combined Normal–Shear–Bending Forces to Natural Sand Grains with Artificial Bonds, Geotechnical Testing Journal, 42(4), 1090-1099. doi: 10.1520/GTJ20170453.

Wang, W., Nardelli, V., Coop, M.R. 2017. Micro-mechanical behaviour of artificially cemented sands under compression and shear, Geotechnique Letters, 7, 218-224.

Wang, Y.H., Leung, S.C. 2008a. A particulate-scale investigation of cemented sand behaviour, Canadian Geotechnical Journal, 45(1), 29-44.

Wang, Y.H., Leung, S.C. 2008b. Characterization of cemented sand by experimental and numerical investigations, Journal of Geotechnical and Geoenvironmental Engineering, 134(7), 992-1004.

Wong, T.F., Baud, P. 2012, The brittle-ductile transition in porous rock: A review, Journal of Structural Geology, 44, 25-53.

Wu, S., Zhang, S., Guo, C., Xiong, L. 2017. A generalized nonlinear failure criterion for frictional materials, Acta Geotechnica, 12, 1353-1371.

Yu, H.S., Tan, S.M., Schnaid, F. 2007. A critical state framework for modelling bonded geomaterials, Geomechanics and Geoengineering: An International Journal, 2(1), 61-74.

586

587 **APPENDIX**

588 **(A) Crushing Load Tests**

589 Crushing tests were conducted on both LBOC and LBPP specimens using a modified CBR apparatus

590 available at City University of Hong Kong. This apparatus was used for single particle crushing tests

591 on various natural geological materials like LBS and CDG (Wang and Coop, 2016). A representative

592 set of 15 samples of each LBOC and LBPP specimens were tested for crushing load. From the method

593 of specimen preparation, it is expected that the LBOC specimens have strong and hard bond while the

594 LBPP specimens have weak and soft bond, and this distinct bond nature influences their crushing loads

595 and behaviour.

596 Figure S2 shows the comparison of load-displacement curves between LBOC and LBPP specimens.

597 The crushing phenomenon was straightforward for LBOC specimens where they showed brittle mode

598 of crushing and there was a sudden drop in the normal load after the first crack was observed, whereas,

599 the LBPP particles showed ductile behaviour with hardening to be observed even after the formation

600 of cracks. A squeezing phenomenon was observed in the plaster as the specimen was compressed and

601 in both the bonding types, it was the bonding material that failed the specimen but not the LBS grains.

602 Wang et al. (2019) also observed a similar phenomenon in crushing artificially bonded LBS gains. The

603 normal load at which the first crack occurred on the OPC bonded particles ($F_N = 220N$) is almost 2

604 times that of PP bonded particles ($F_N = 114N$) but for a given normal load below the crushing load,

605 the displacement is always higher for LBPP than LBOC. The higher strength and stiffness for OPC

606 bonded particles qualifies them to be 'strong and hard cementation' while the lower strength and

607 stiffness for PP bonded particles qualifies them to be 'weak and soft cementation'.

608 **(B) Tensile Load Tests**

609 Tensile load tests were conducted on the new micromechanical loading apparatus (Section 3). The top

610 and bottom grains of the specimen were glued to the respective mounts on the apparatus with a

611 minimum normal load applied (around 0.1N) to ensure firm contact between the specimen and the

612 mounts. After the preparation of the cemented samples, the extension tests were conducted to measure

613 the tensile strength of the specimens. In general, these tests showed a brittle behavior with a sudden

614 drop of the load after reaching a peak value. The average tensile load at which the bond breakage

615 occurred for LBOC specimens was 1.71N and the breakage occurred at a very low extension of around

616 1.25μm indicating the brittle nature of the bond. The normal load-extension curve for a representative

617 specimen is shown in Figure S3. While, the LBPP particles did not show any recordable tensile load

618 during the separation of the bonding.

619

620 **List of Figures**

621 Figure 1: (a) Microscopic image of top surface of flattened LBS grain (b) Surface profile from
622 interferometry analysis. Representative EDS spectrum of (c) Plaster of Paris (d) Ordinary Portland
623 cement with inset of the figures showing SEM images of the corresponding materials.
624
625 Figure 2: (a) Upgraded micromechanical testing apparatus for cemented grains; (b) Horizontal loading
626 system; (c) Vertical loading system; (d) Close-up view of arrangement of specimen for testing.
627
628 Figure 3: Tangential load – displacement behaviour of LBOC and LBPP specimes (a)-(b) Zero normal
629 load; (c)-(d) Low-medium normal load; (e)-(f) Medium to high normal load.
630
631 Figure 4: Variation of peak tangential load (left axis) and load ratio (right axis) with normal load for
632 (a) LBOC and (b) LBPP specimens. (c) Fitting of nonlinear strength envelope for experimental data.
633
634 Figure 5: Tangential stiffness degradation curves for LBOC and LBPP specimens at (a) and (c) low to
635 medium and, (b) and (d) medium to high normal loads.

636
637 Figure 6: (a)-(b) Tangential load – displacement curves for first cycle of shearing of LBOC specimens;
638 (c) Representative curve of normal displacement versus tangential displacement under cyclic shearing
639 at 25N normal load.
640
641 Figure 7: Tangential load – displacement curves under five cycles of shearing (a) 25N – 0.01mm (b)
642 50N – 0.01mm (c) 25N – 0.025mm
643
644 Figure 8: (a) Variation of ratio of energy dissipated in a cycle to first cycle of shearing (b) Variation
645 of hysteretic damping ratio from cycle to cycle at three test conditions (c) Variation of tangential load
646 amplitude from cycle to cycle.
647
648

649 Figure 9: (a) Variation of normal displacement (dilation or compression) with shearing displacement
650 at different normal loads for LBOC specimens; (b) Comparison of variation of tangential load, normal
651 load and normal displacement with shearing displacement for F_N = 8N test; (c)Variation of rate of
652 dilation or compression with shearing displacement; (d) Variation of normal displacement (dilation or
653 compression) with shearing displacement at different normal loads for LBPP specimens.
654
655 Figure 10: (a) Stages of mode-1 failure of LBOC specimens at lower normal loads. (b) Breakage
656 phenomena at three ranges of normal loads for LBPP specimens.
657
658 Figure 11: Relation between load ratio and rate of dilation at low, medium and high normal loads.
659
660 Figure S1: Representative tangential load – displacement curves indicating changes in load –
661 displacement curves relating to breakage phenomenon.
662
663 Figure S2: Representative normal load-displacement curves for LBOC and LBPP specimens in
664 crushing.
665
666 Figure S3: Representative normal load-displacement curve for LBOC specimen under extension
667 (tensile load).
668

669

670 **List of Tables**

671 Table 1: Monotonic shearing test details and preliminary results

672 Table 2: Observations from cyclic shearing tests on LBOC specimens.

673 Table 3: Qualitative summary of bonded grains behaviour
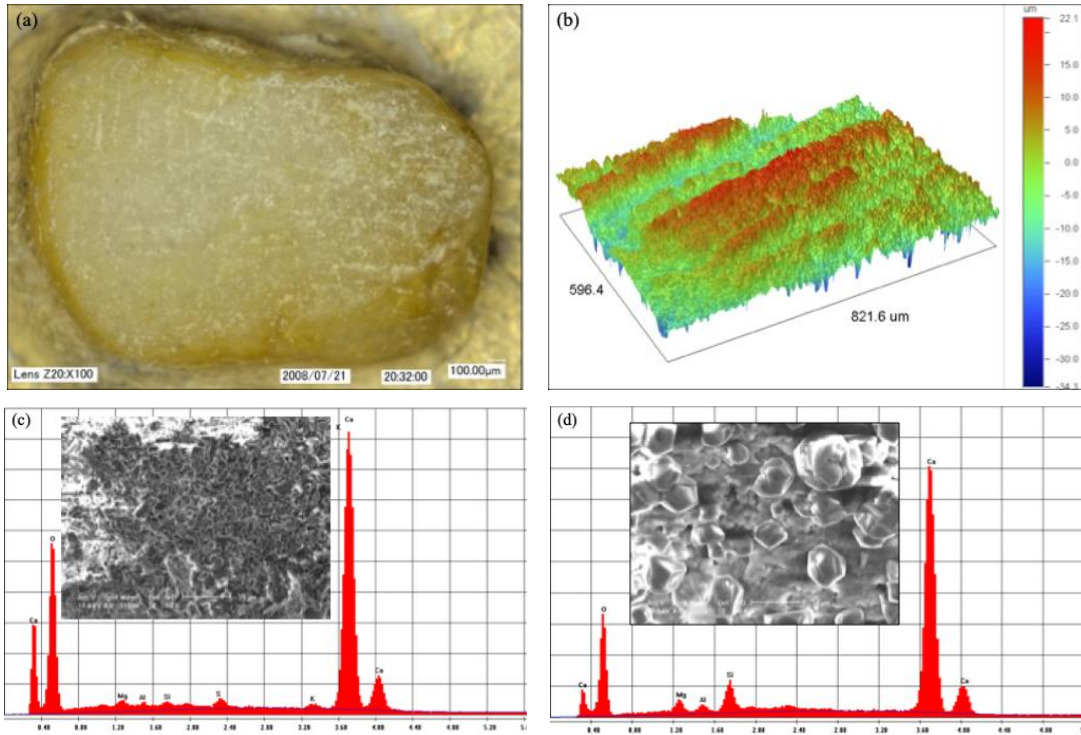
Figure 1: (a) Microscopic image of top surface of flattened LBS grain (b) Surface profile from interferometry analysis. Representative EDS spectrum of (c) Plaster of Paris (d) Ordinary Portland cement with inset of the figures showing SEM images of the corresponding materials.

690
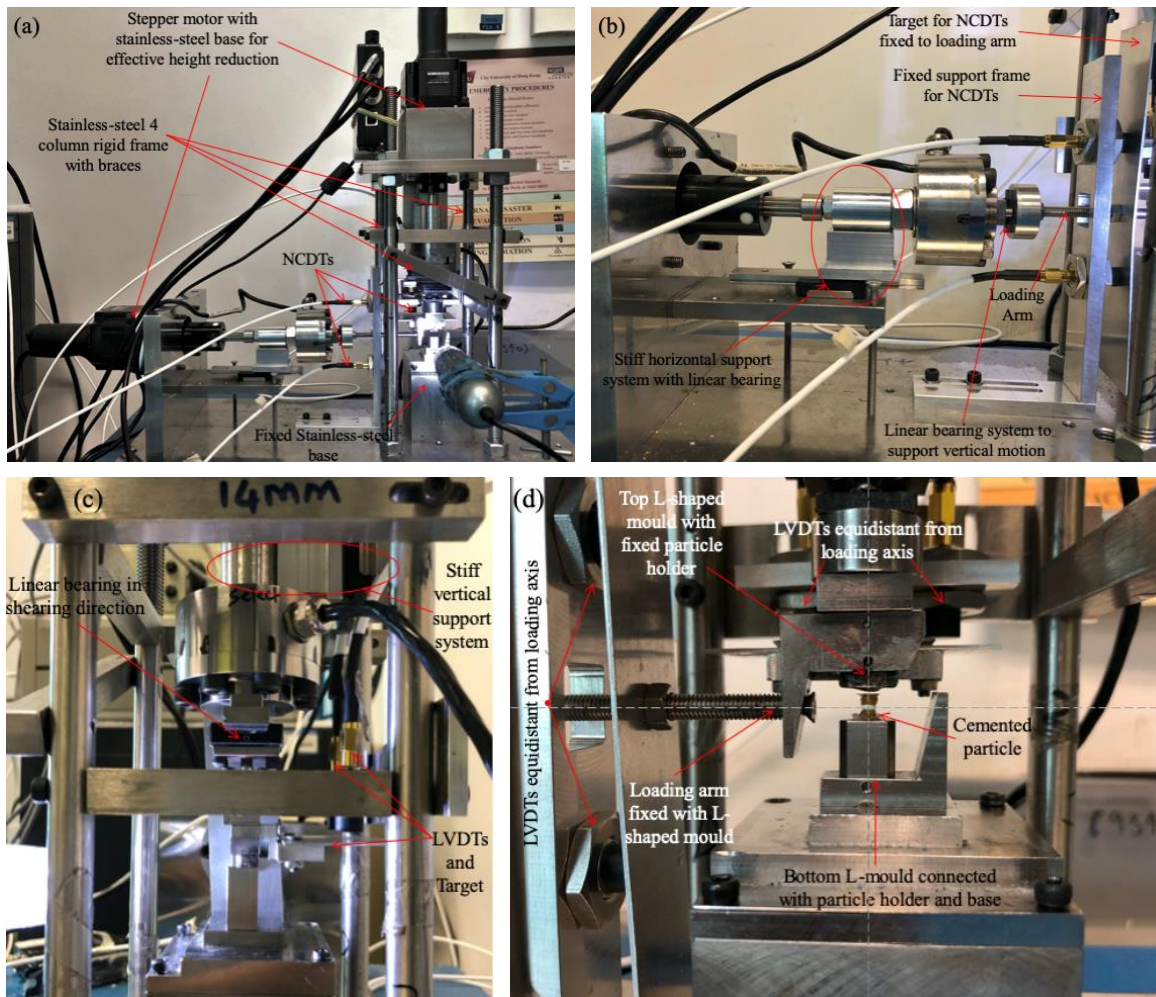
691

692   Figure 2: (a) Upgraded micromechanical testing apparatus for cemented grains; (b) Horizontal
693   loading system; (c) Vertical loading system; (d) Close-up view of arrangement of specimen for
694   testing.
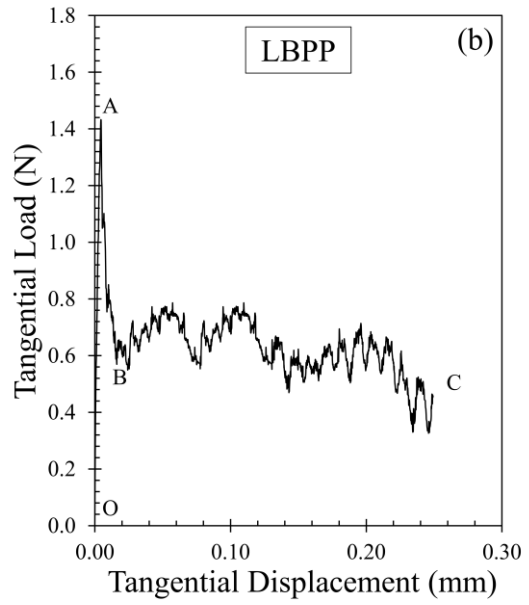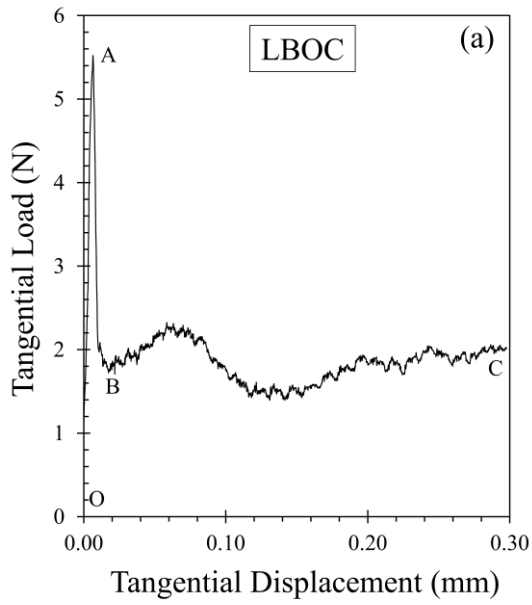
695

696

697

698

699

34
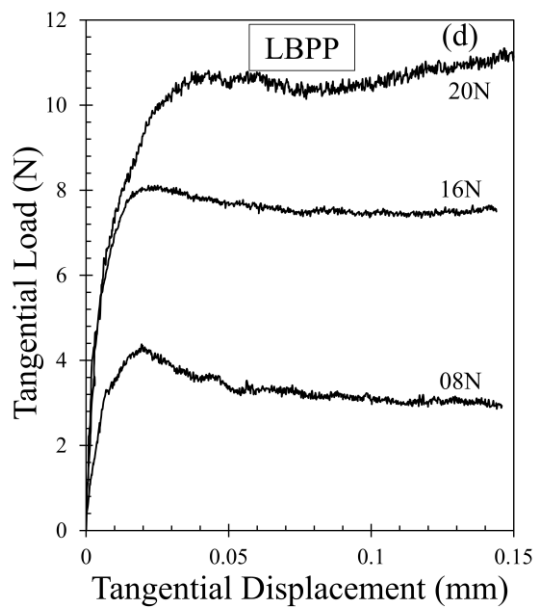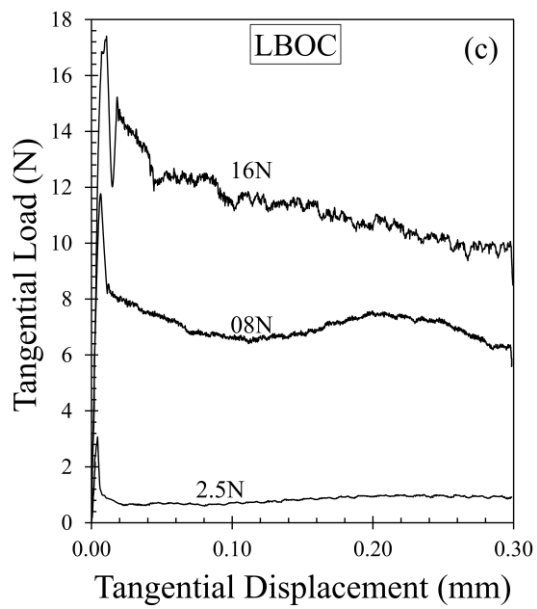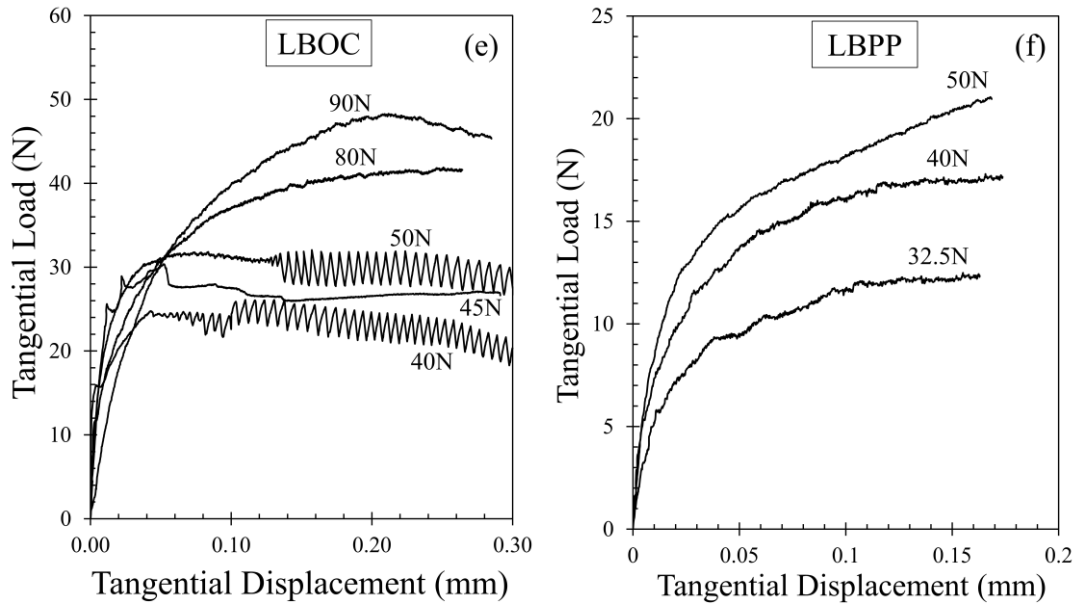
Figure 3: Tangential load – displacement behaviour of LBOC and LBPP specimes (a)-(b) Zero normal load; (c)-(d) Low-medium normal load; (e)-(f) Medium to high normal load.
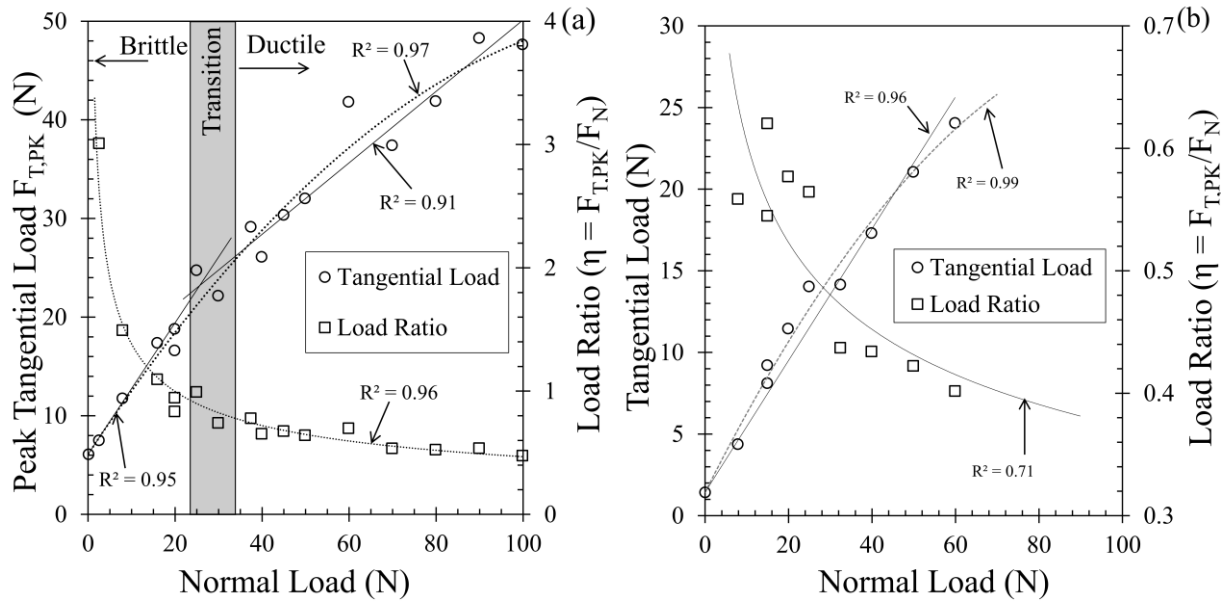
719
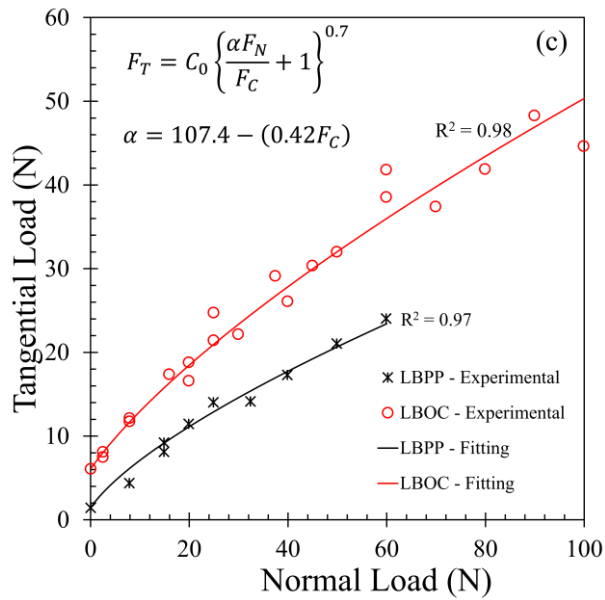
720

Figure 4: Variation of peak tangential load (left axis) and load ratio (right axis) with normal load for (a) LBOC and (b) LBPP specimens. (c) Fitting of nonlinear strength envelope for experimental data.

724
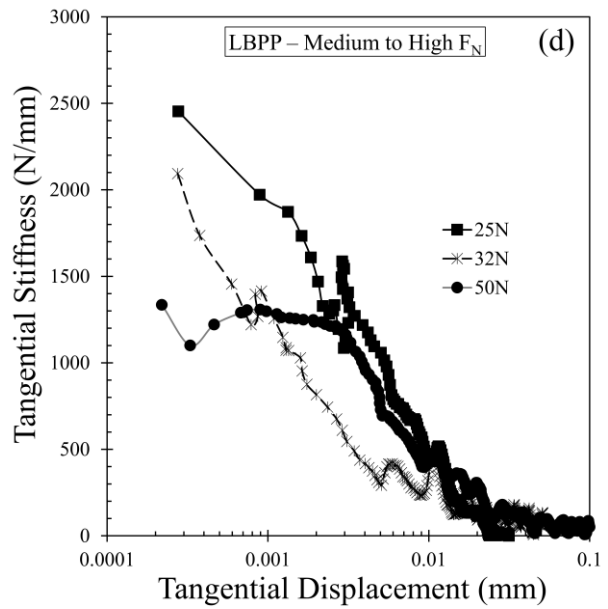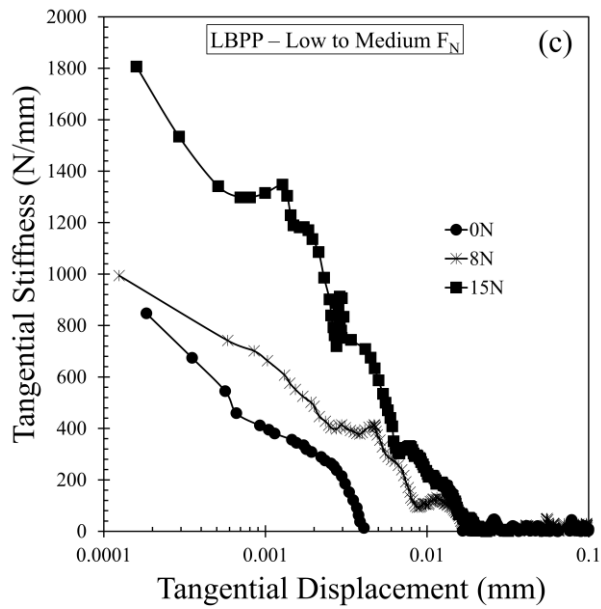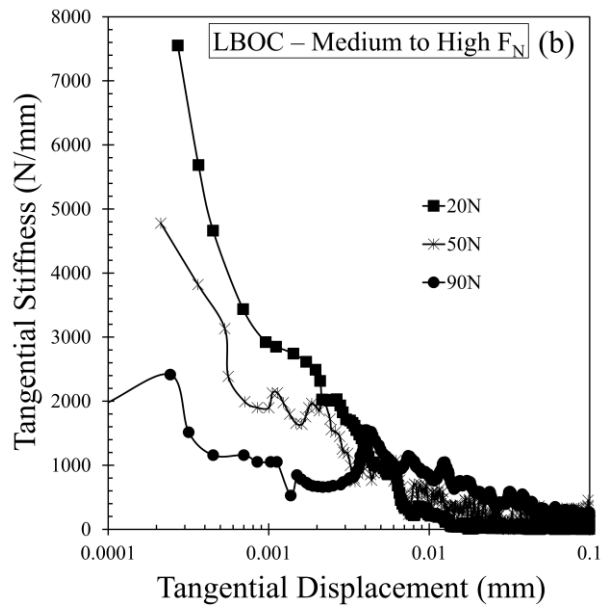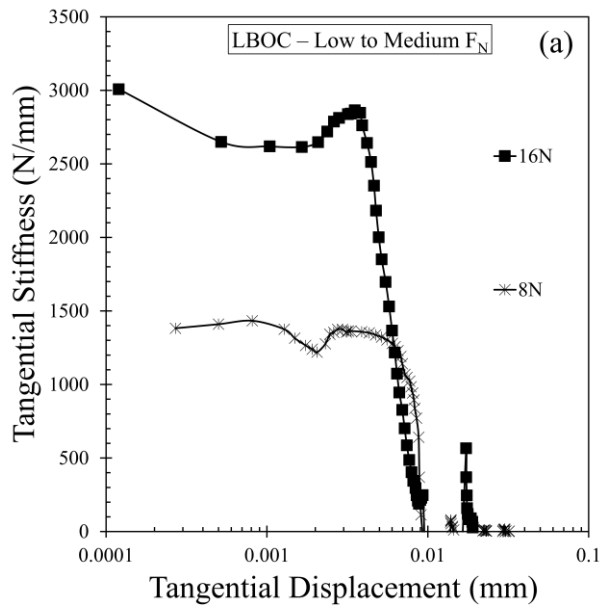
725

Figure 5: Tangential stiffness degradation curves for LBOC and LBPP specimens at (a) and (c) low to medium and, (b) and (d) medium to high normal loads.
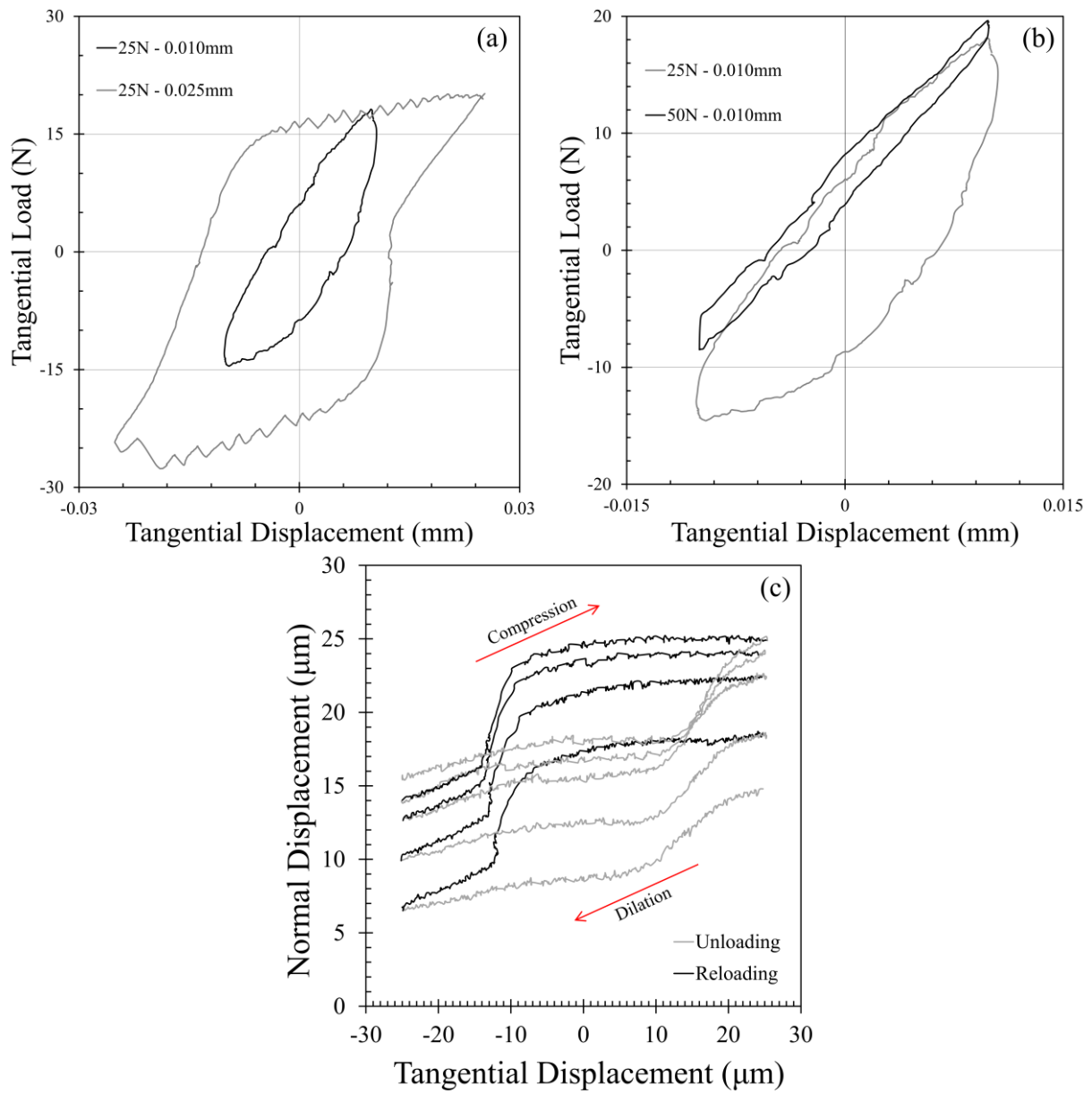
729

730

Figure 6: (a)-(b) Tangential load – displacement curves for first cycle of shearing of LBOC
specimens; (c) Representative curve of normal displacement versus tangential displacement under
cyclic shearing at 25N normal load.
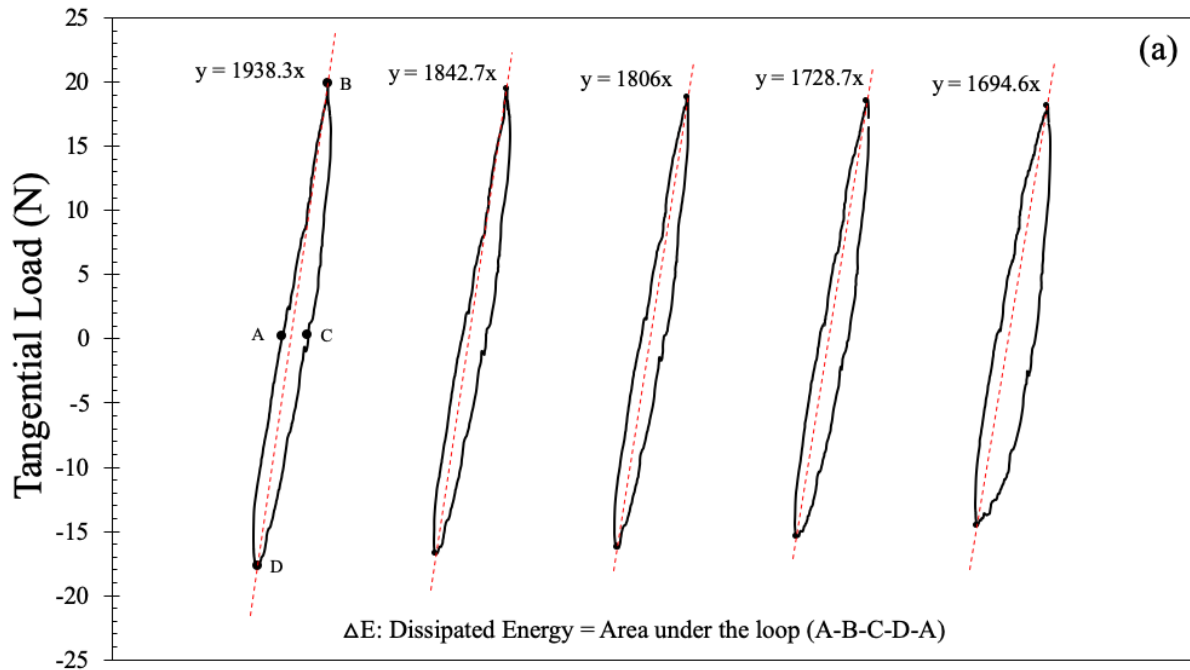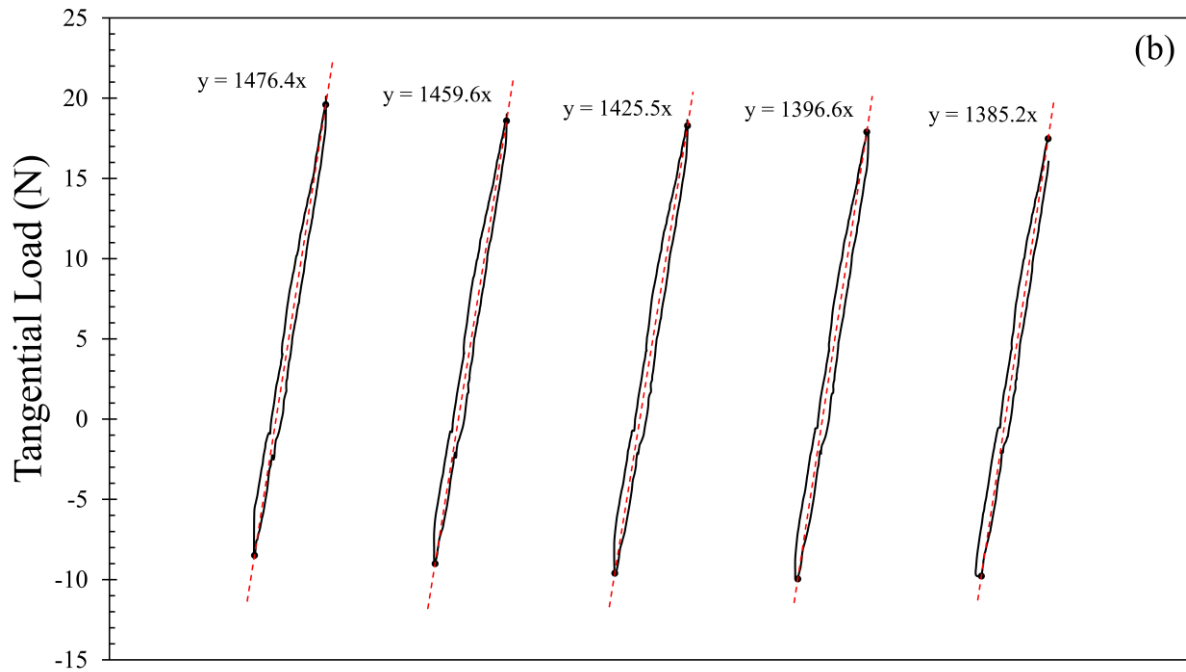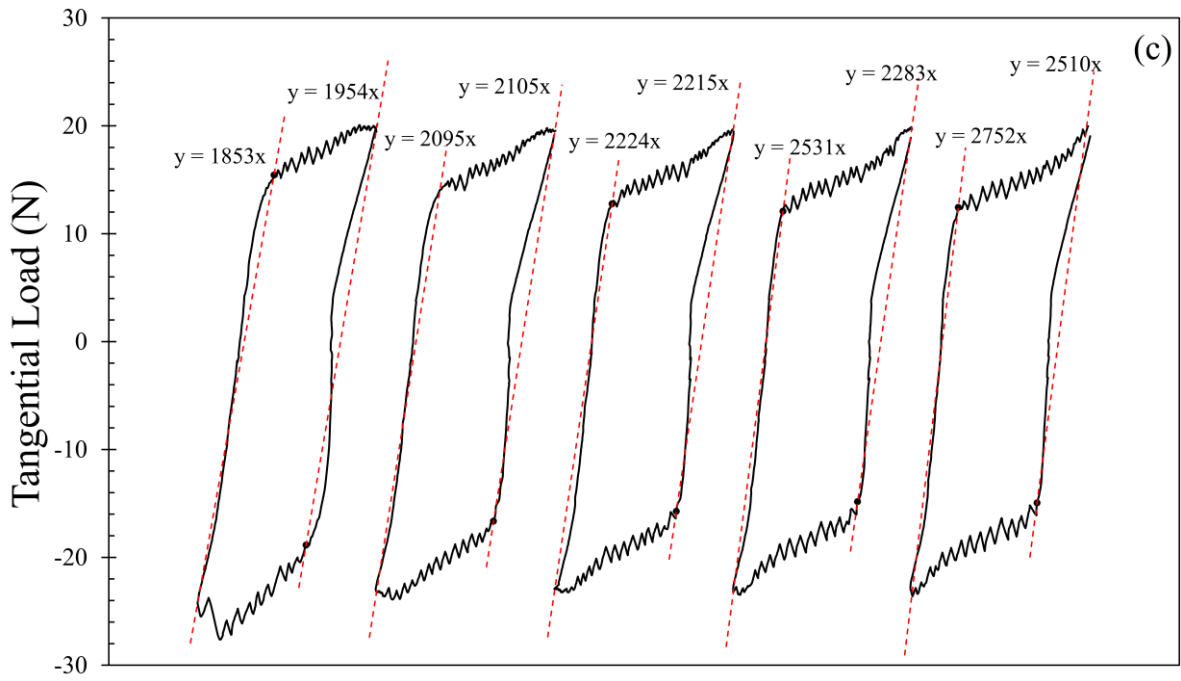
Figure 7: Tangential load – displacement curves under five cycles of shearing (a) 25N – 0.01mm (b) 50N – 0.01mm (c) 25N – 0.025mm
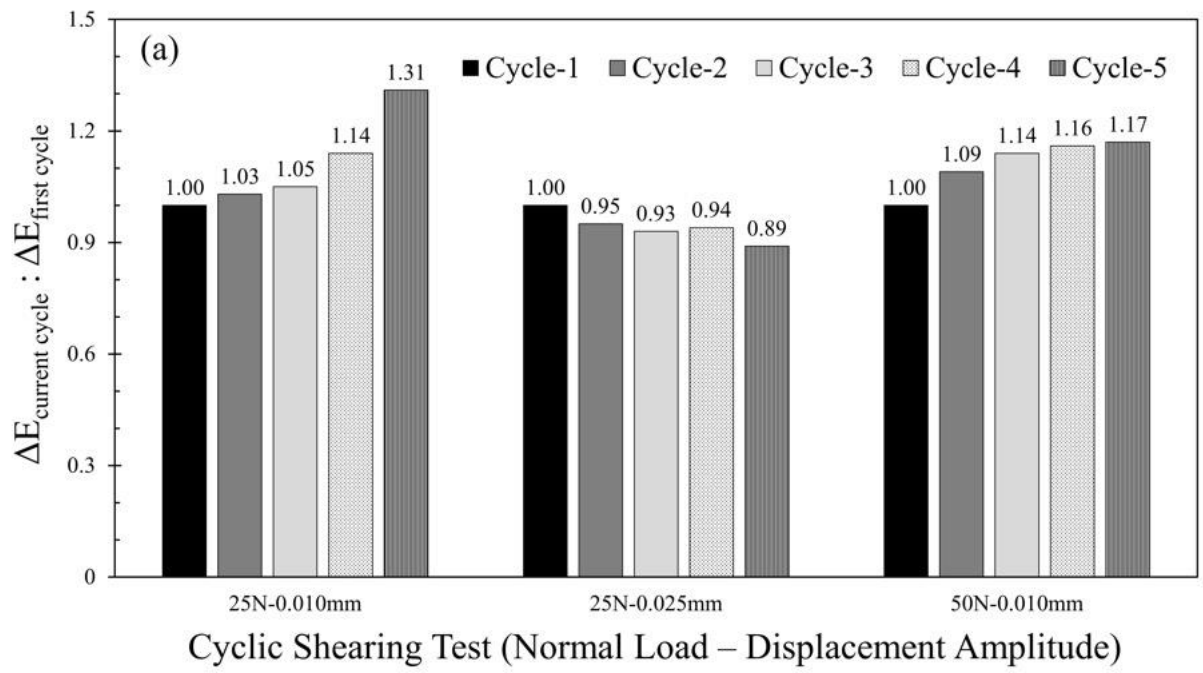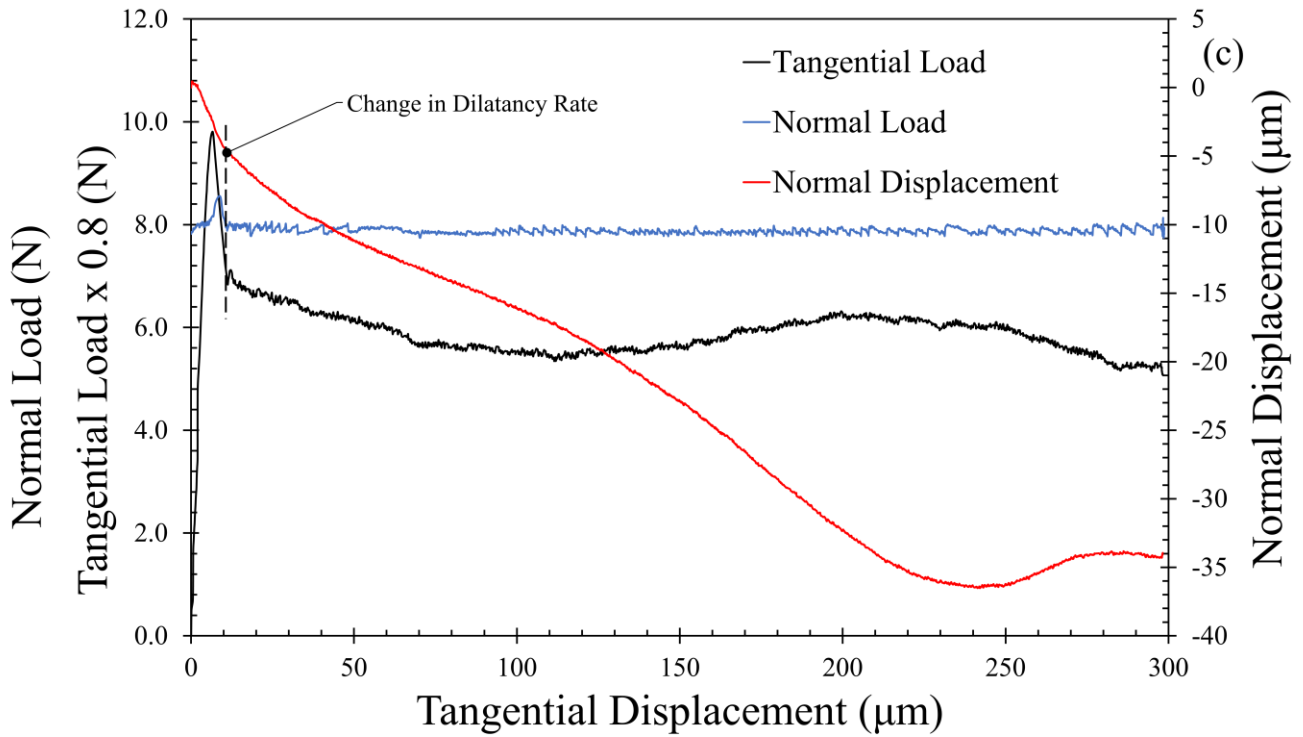
748
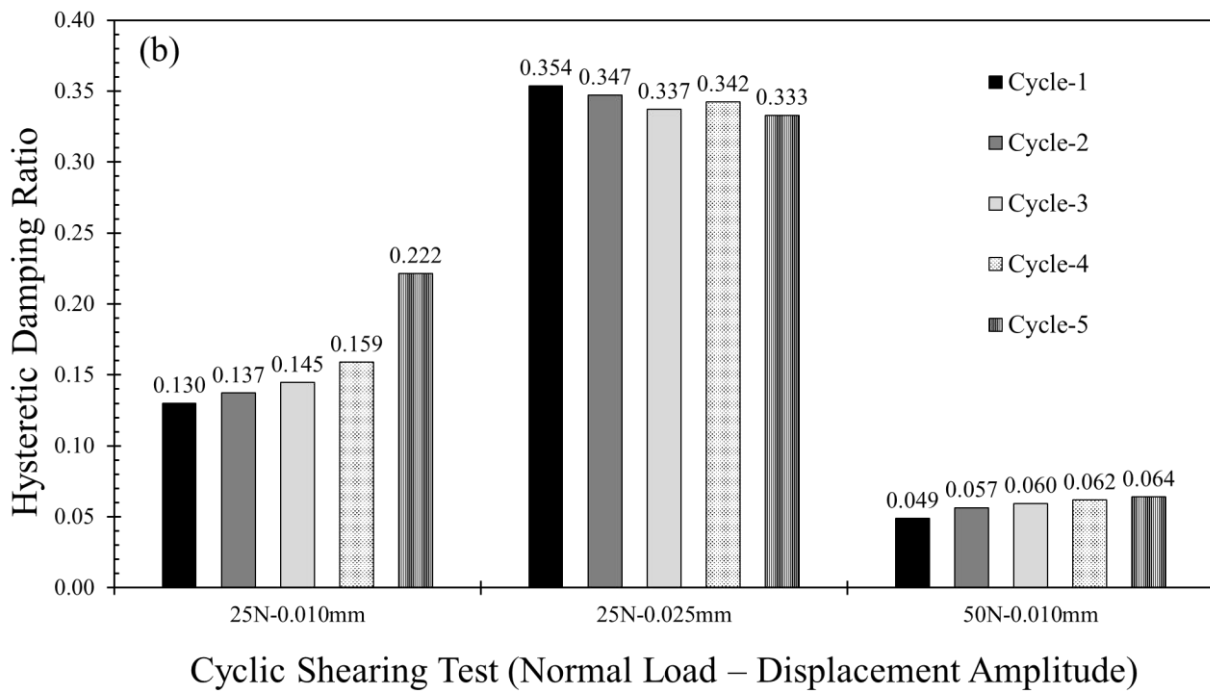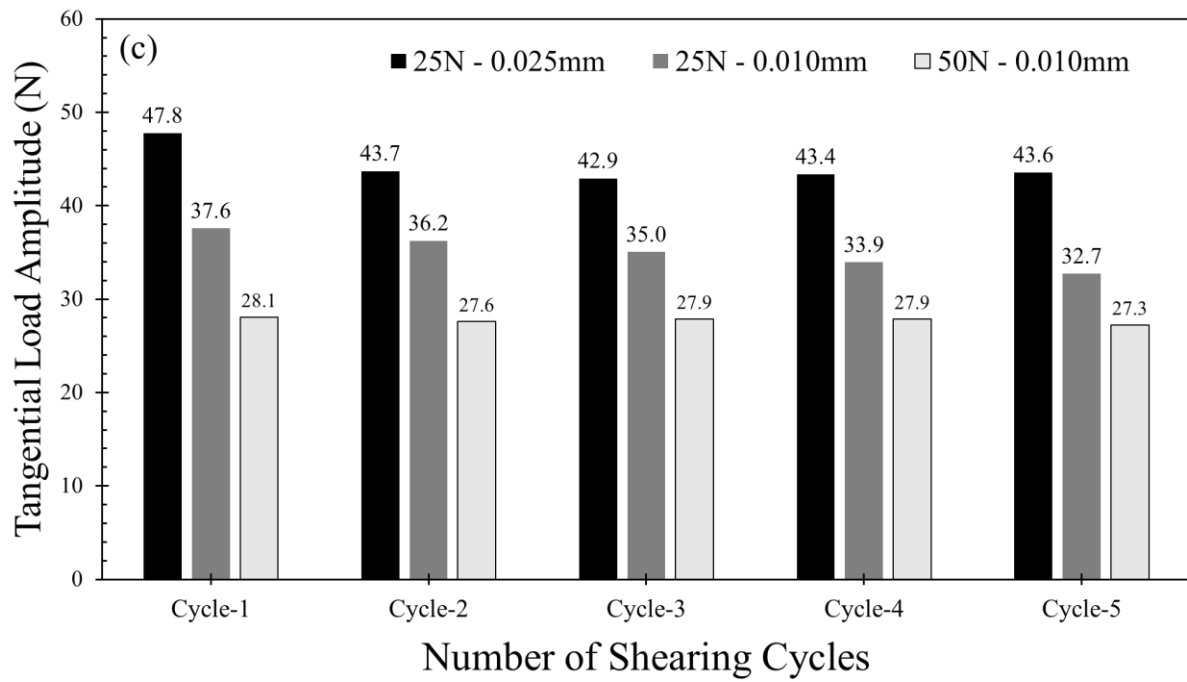
749

750

751

752

753

Figure 8: (a) Variation of ratio of energy dissipated in a cycle to first cycle of shearing (b) Variation of hysteretic damping ratio from cycle to cycle at three test conditions (c) Variation of tangential load amplitude from cycle to cycle.

759
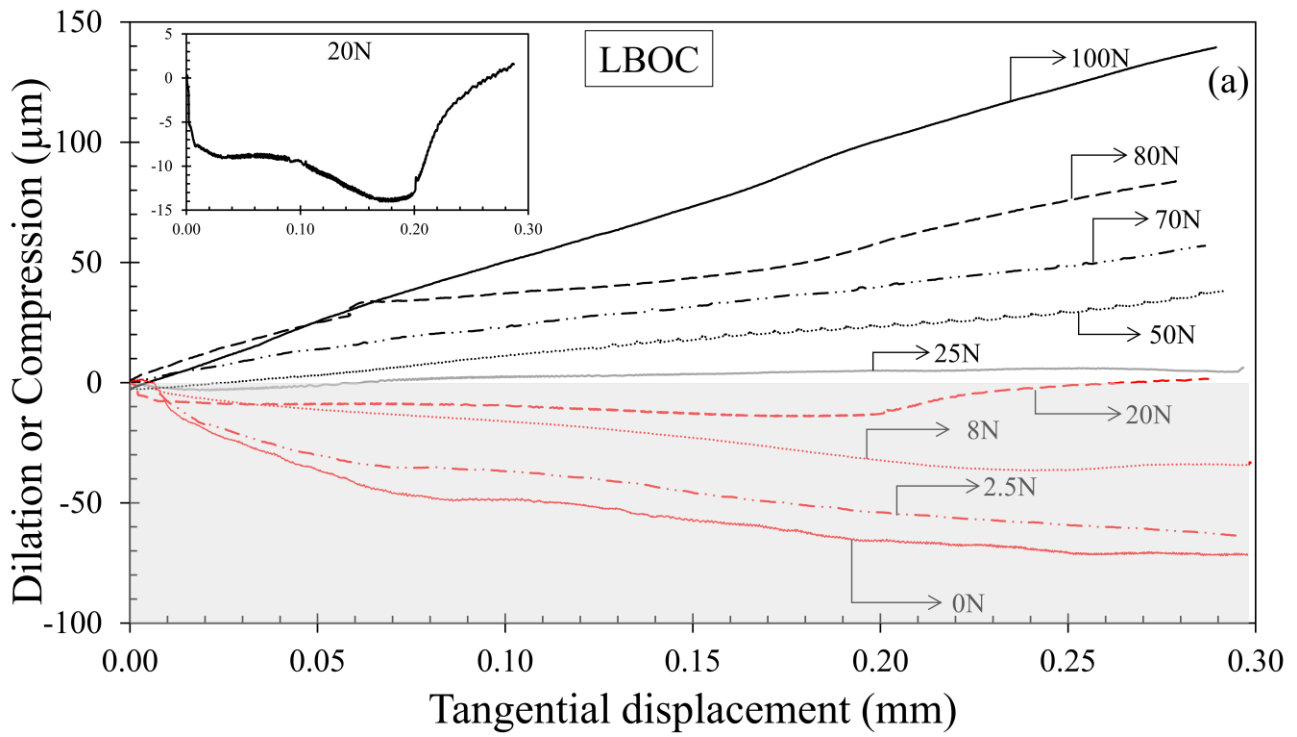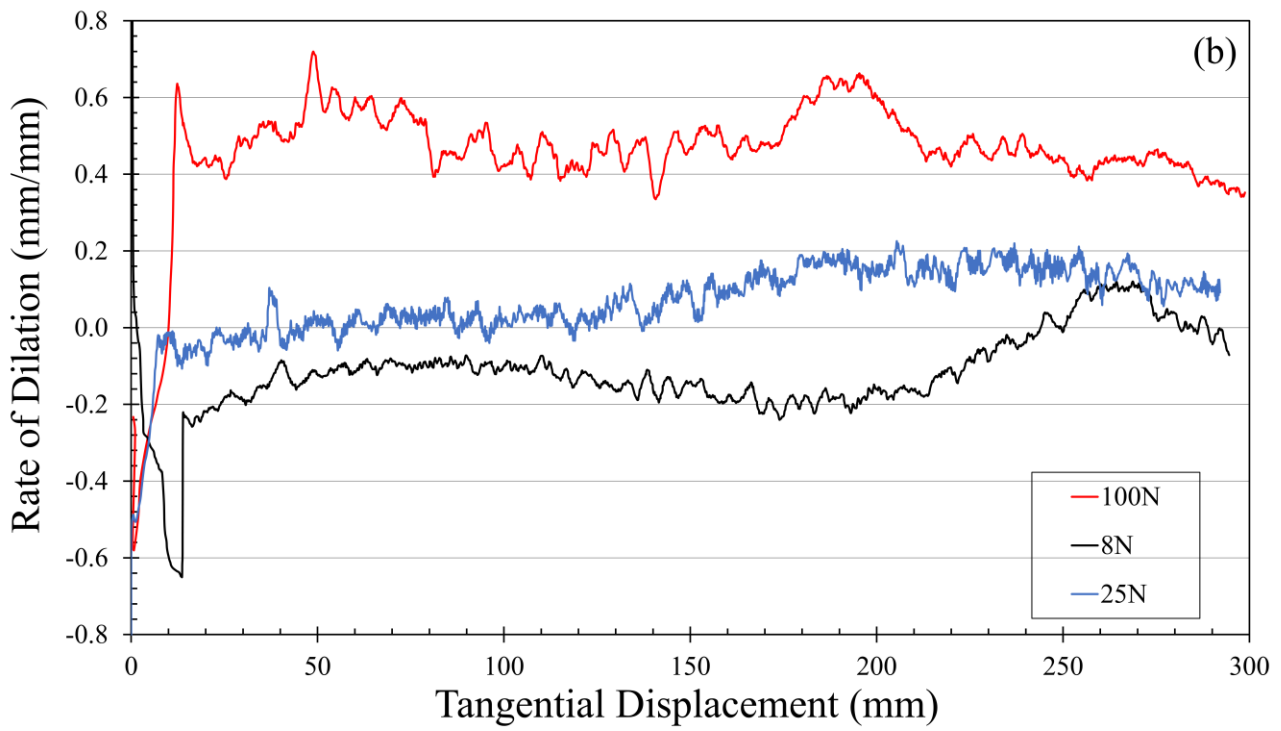
760
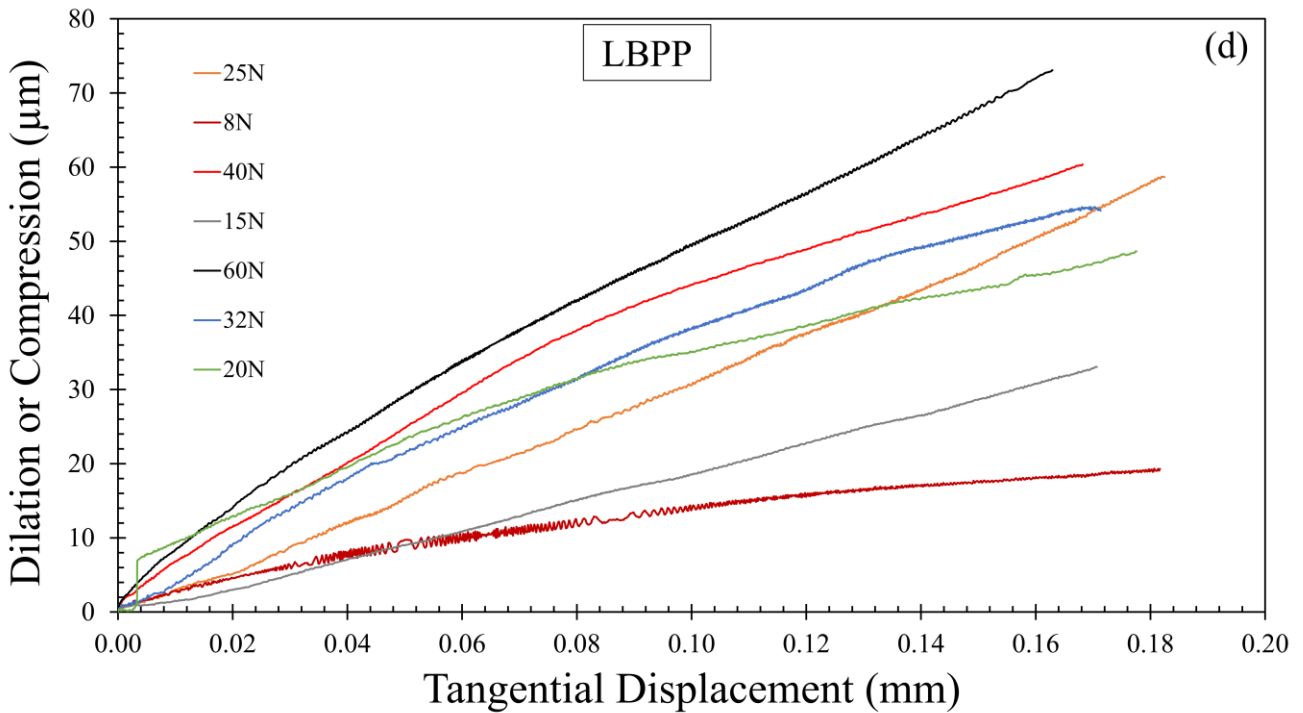
761

762
763 Figure 9: (a) Variation of normal displacement (dilation or compression) with shearing displacement
764   at different normal loads for LBOC specimens; (b) Comparison of variation of tangential load,
765   normal load and normal displacement with shearing displacement for F_N = 8N test; (c)Variation of
766   rate of dilation or compression with shearing displacement; (d) Variation of normal displacement
767   (dilation or compression) with shearing displacement at different normal loads for LBPP specimens.
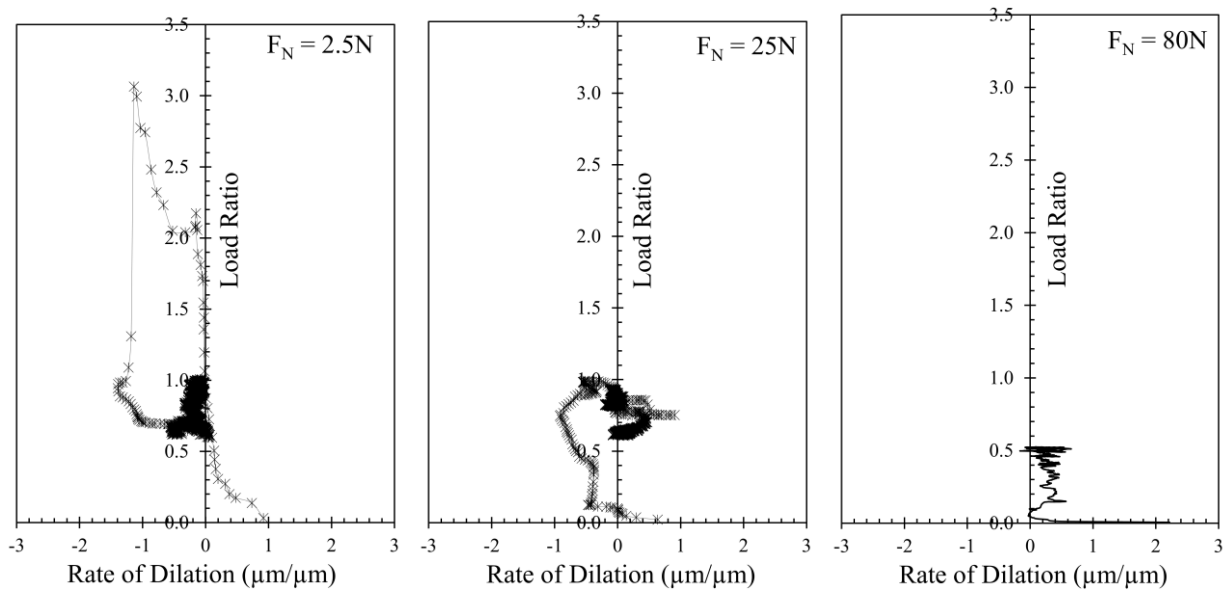768
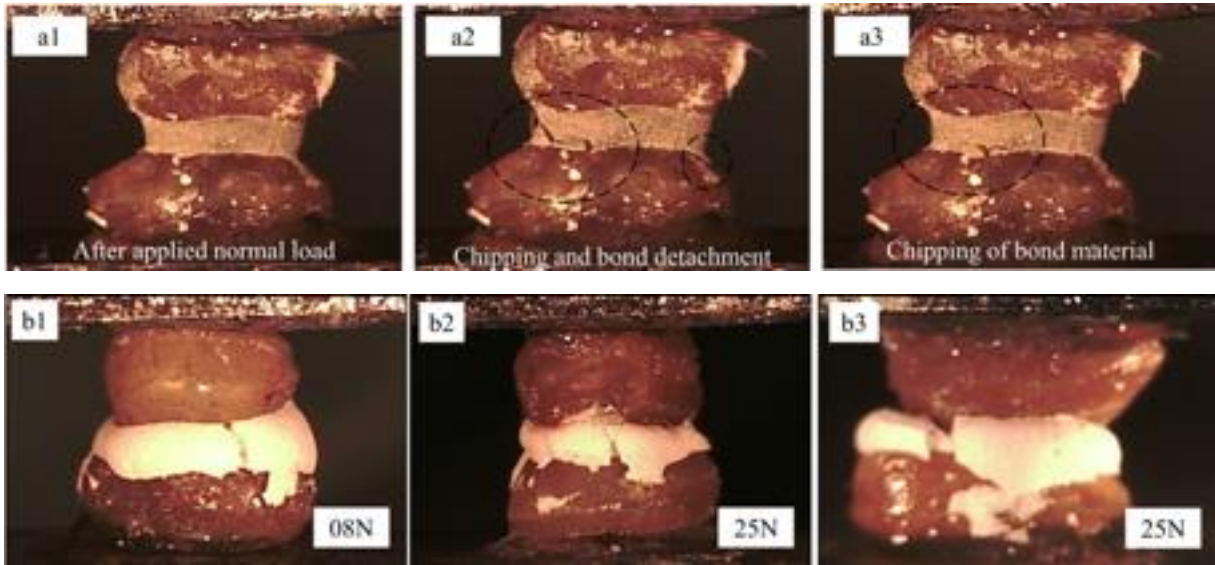
770

771

Figure 10: (a) Stages of mode-1 failure of LBOC specimens at lower normal loads. (b) Breakage phenomena at three ranges of normal loads for LBPP specimens.
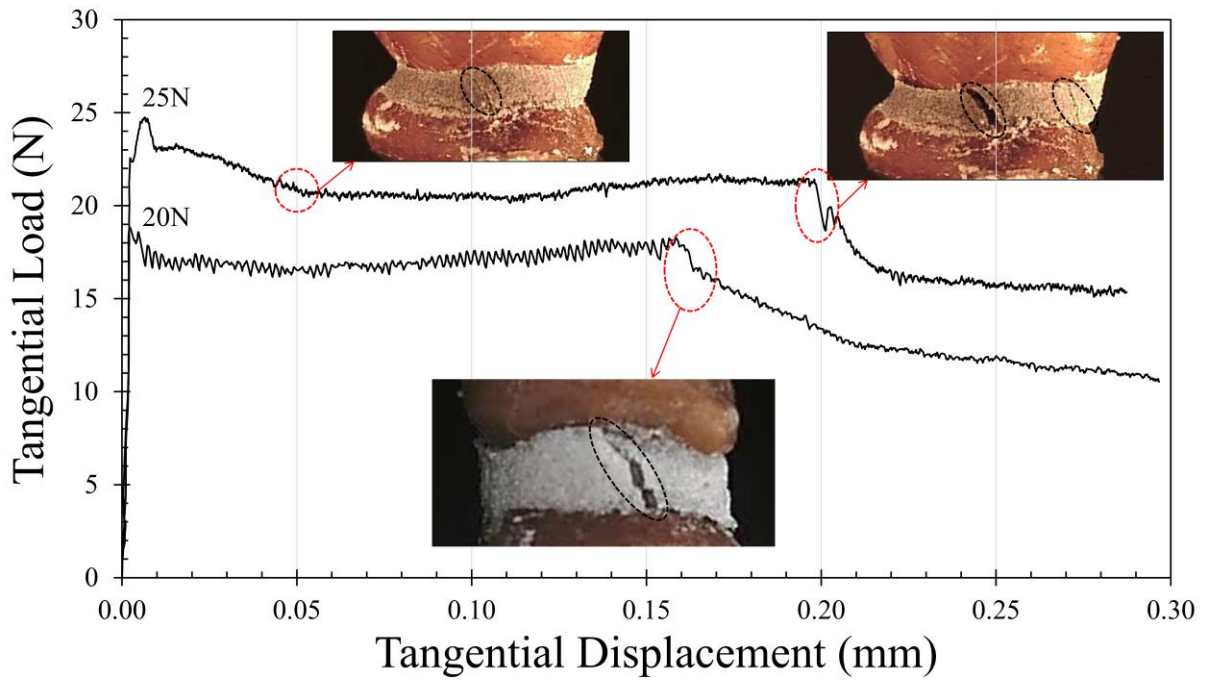
774

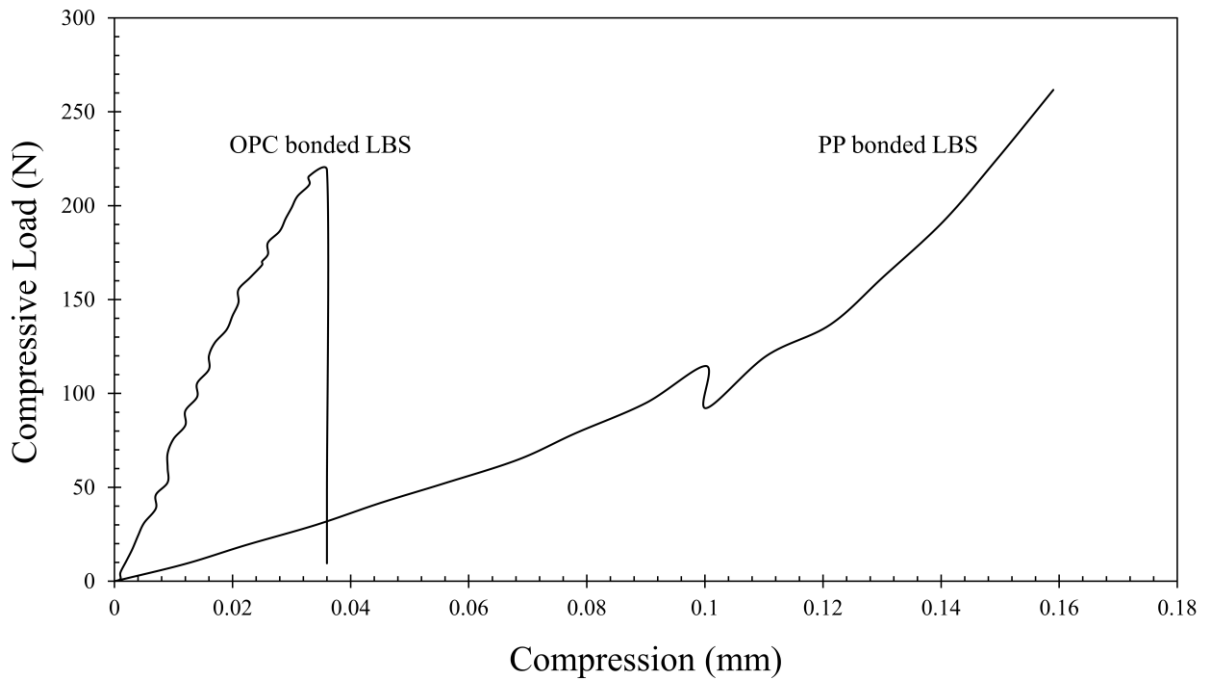
775

Figure 11: Relation between load ratio and rate of dilation at low, medium and high normal loads.

777

778

Figure S1: Representative tangential load – displacement curves indicating changes in load – displacement curves relating to breakage phenomenon.

779
780
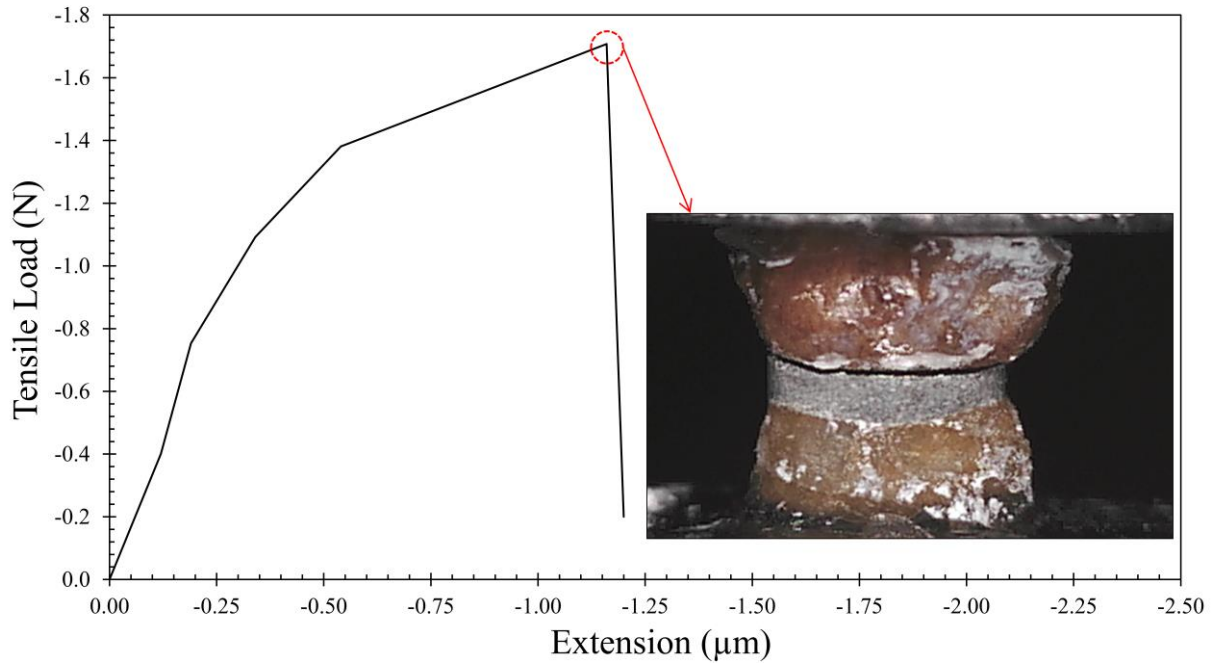781

782

Figure S2: Representative normal load-displacement curves for LBOC and LBPP specimens in crushing.

783
784
785
786

787

Figure S3: Representative normal load-displacement curve for LBOC specimen under extension
(tensile load)

Bonding Material (Code)	Normal Load (N)	Tangential Load (N)		Load Ratio (F_T/F_N)		Dilation (or) Compression
		Peak	Steady-state	Peak	Steady-state	
Ordinary Portland Cement (LBOC)	0	5.5	1.8	-	-	Dilation
	2.5	7.5	2.1	3.00	0.84	
	8	11.8	6.5	1.48	0.81	
	16	17.4	9.9	1.09	0.62	
	20	18.8	16.1	0.94	0.81	Post-fracture compression
	25	24.5	21.5	0.98	0.86	
	30	22.2		0.74		Compression
	37.5	29.2		0.78		
	40	26.1		0.65		
	45	30.4		0.68		
	50	32.0		0.64		
	60	42.5		0.71		
	70	37.4		0.53		
	80	41.9		0.52		
	90	48.3		0.54		
	100	44.7		0.45		
Plaster of Paris (LBPP)	0	1.4	0.6	-	-	Dilation
	8	4.4	3.1	0.55	0.39	Compression
	15	8.1	7.4	0.54	0.49	
	20	11.5		0.58		
	25	14.0		0.56		
	32.5	14.2		0.44		
	40	17.3		0.43		
	50	21.1		0.42		
	60	28.5		0.48		

792

Table 2: Observations from cyclic shearing tests on LBOC specimens.

Normal Load (N)	Displacement Amplitude (mm)	Cycle	Energy Dissipated (N-mm)	Damping Ratio	Stiffness (N/mm)	Load Amplitude (N)
25N	0.010	1	0.1628	0.130	1938.3	37.56
		2	0.1678	0.137	1842.7	36.24
		3	0.1708	0.145	1806	35.03
		4	0.1851	0.159	1728.7	33.93
		5	0.2526	0.222	1694.6	32.71
25N	0.025	1	1.1193	0.345	1903.5	47.8
		2	1.0661	0.347	2100	43.7
		3	1.0420	0.337	2219.5	42.9
		4	1.0466	0.362	2407	43.4
		5	0.9962	0.333	2631	43.6
50N	0.010	1	0.0602	0.049	1476.4	28.08
		2	0.0660	0.057	1459.6	27.6
		3	0.0684	0.060	1425.5	27.88
		4	0.0696	0.062	1396.6	27.87
		5	0.0703	0.064	1385.2	27.25

794

795

796   Table 3: Qualitative summary of bonded grain behaviour

Specimen	Normal Load (N)	Volumetric Behaviour	Breakage Mode		Tangential Behaviour	
					Mode	Reference
LBOC (Hard and strong bond)	0-16	Dilation	Chipping and specimen separation	Brittle	Softening	Figure 3a & Figure 3c
	20-30	Zero dilation and Post-fracture compressison	Shear cracks and Splitting	Brittle – Ductile Transition	Minor softening	Figure S1
	40-100	Compression	Crushing	Ductile	Hardening	Figure 3e
LBPP (Soft and weak bond)	0	Dilation	No damage to bonding material		Softening	Figure 3b
	8-15	Compression	Crushing and sqeezing of soft bonding material.		Minor softening	Figure 3d
	20-60				Hardening	Figure 3f

797